Article
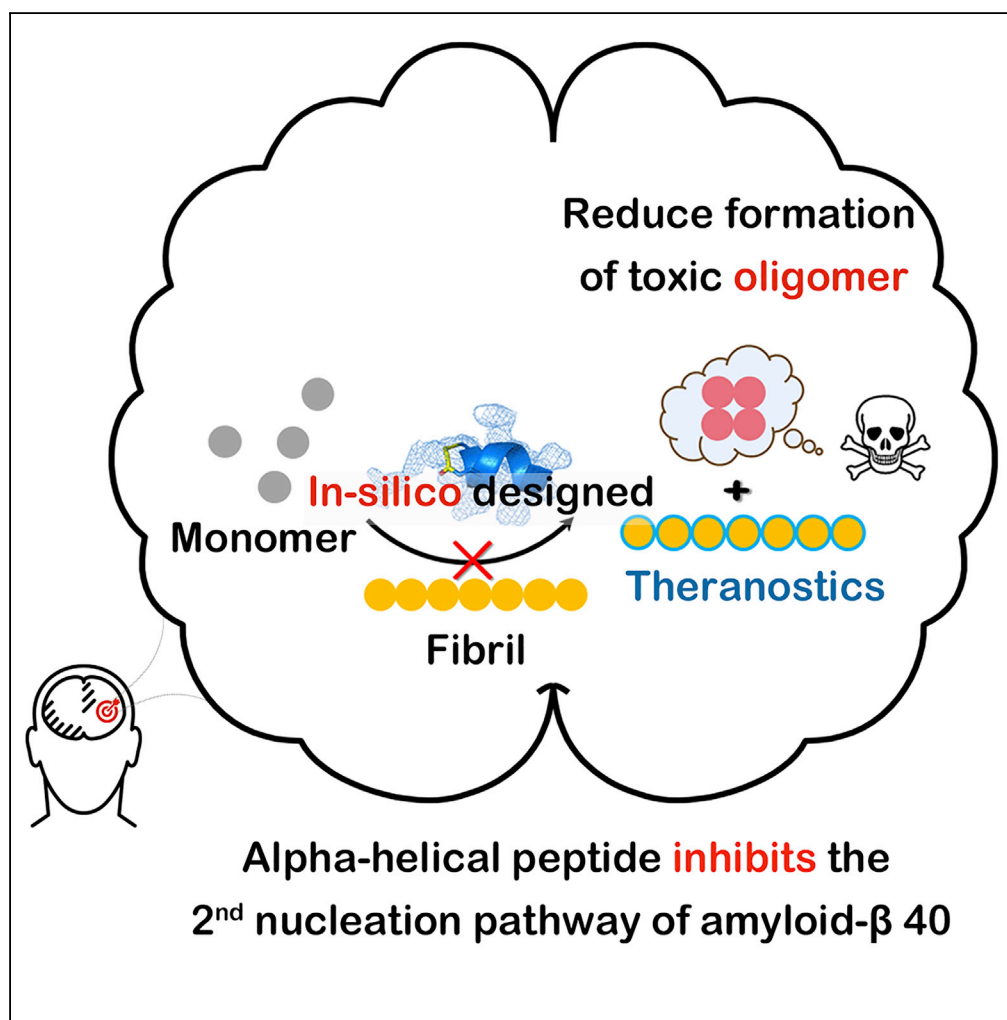
α-Helical Motif as Inhibitors of Toxic Amyloid-β Oligomer Generation via Highly Specific Recognition of Amyloid Surface

Yixiang Jiang,
Xuehan Jiang,
Xiaodong Shi, ...,
Feng Yin, Wei
Han, Zigang Li

yinfeng@pkusz.edu.cn (F.Y.)
hanw@pkusz.edu.cn (W.H.)
lizg@pkusz.edu.cn (Z.L.)

HIGHLIGHTS

Demonstrating that alpha-helical motif specifically recognizes Aβ amyloid surface

In silico structure-based design of peptides as PPI blockers

Disrupting Aβ-fibril interaction to prevent toxic oligomer formation

CellPress

Article

α-Helical Motif as Inhibitors of Toxic Amyloid-β Oligomer Generation via Highly Specific Recognition of Amyloid Surface

Yixiang Jiang,[1,2,3] Xuehan Jiang,[1,3] Xiaodong Shi,[1] Fadeng Yang,[1] Yang Cao,[1] Xuan Qin,[1] Zhanfeng Hou,[1] Mingsheng Xie,[1] Na Liu,[1] Qi Fang,[1] Feng Yin,[1,2,*] Wei Han,[1,*] and Zigang Li[1,2,4,*]

SUMMARY

Amyloid fibril surfaces can convert soluble proteins into toxic oligomers and are attractive targets for intervention of protein aggregation diseases. Thus far, molecules identified with inhibitory activity are either large proteins or flat cyclic compounds lacking in specificity. The main design difficulty is flatness of amyloid surfaces and the lack of knowledge on binding interfaces. Here, we demonstrate, for the first time, a rational design of alpha-helical peptide inhibitors targeting the amyloid-beta 40 (Aβ40) fibril surfaces, based on our *in silico* finding that a helical fragment of Aβ40 interacts in a unique way with side-chain arrays on the fibril surface. We strengthen the fragment's binding capability through mutations and helicity enhancement with our Terminal Aspartic acid strategy. The resulting inhibitor shows micromolar affinity for the fibril surface, effectively impedes the surface-mediated oligomerization of Aβ40, and mitigates its cytotoxicity. This work opens up an avenue to designing aggregation modulators for amyloid diseases.

INTRODUCTION

Soluble peptides or proteins can misfold and self-assemble into highly ordered aggregates, which have garnered tremendous interest, as they are implicated in protein conformational diseases that range from neurodegenerative disorders to systemic amyloidosis (Chiti and Dobson, 2006). A key hallmark of such diseases is amyloid fibril deposition (Tycko, 2011). Structurally, these fibrils are characterized by highly repetitive packing of identical peptide chains in extended β-sheets (Tycko, 2011). Owing to the close relationship between protein self-assembly and the etiology of multiple diseases, there has been a longstanding, therapeutic interest in preventing this process.

Alzheimer disease is the most common neurodegenerative disorder and is characterized by the self-assembly of a 40- to 42-amino acid amyloid-beta (Aβ) peptide into amyloid fibrils (Lorenzo and Yankner, 1994). Previous studies have shown that the Aβ assembly process comprises a series of microscopic events involving protein-protein interactions (PPIs) between various molecular species, including monomers, oligomers, and fibrillar aggregates. These events contribute in different extents to the overall kinetics of converting soluble Aβ into amyloid fibrils (Meisl et al., 2017). Therefore, associated PPIs are the likely targets for inhibiting Aβ assembly (Arosio et al., 2014a, 2014b). Many research groups focus on screening inhibitors that can block or reverse this overall assembly process to alleviate the associated toxicity (Bartolini and Andrisano, 2010; Härd and Lendel, 2012).

As an alternative, structure-based rational design employs structural information of the binding interface to assist in inhibitor construction. This approach has proven particularly effective in the design of PPI inhibitors (Azzarito et al., 2013). However, this structure-based approach to the discovery of protein self-assembly inhibitors is limited by both the complexity of the assembly process and the experimental difficulty in characterizing the structural details of PPIs pertaining to individual microscopic events during the assembly process (Habchi et al., 2017; Munke et al., 2017). So far, there have been a few examples of inhibitor design of inhibitors for Aβ self-assembly (Doig and Derreumaux, 2015; Goyal et al., 2017). Depending on their specific binding modes, these compounds block fibril growth, prevent lateral association of fibrils, or shift the equilibrium toward non-toxic fibrillar aggregates (Jiang et al., 2013; Sievers et al., 2011; Soto et al., 1998).

Recent experimental and theoretical studies have revealed that a fibril's surface can greatly facilitate the conversion of soluble Aβ into oligomeric species (Arosio et al., 2014a, 2014b; Cohen et al., 2013; Meisl

[1]State Key Laboratory of Chemical Oncogenomics, School of Chemical Biology and Biotechnology, Shenzhen Graduate School of Peking University, Shenzhen 518055, China

[2]Shenzhen Bay Laboratory, Shenzhen 518055, China

[3]These authors contributed equally

[4]Lead Contact

*Correspondence:
yinfeng@pkusz.edu.cn (F.Y.),
hanw@pkusz.edu.cn (W.H.),
lizg@pkusz.edu.cn (Z.L.)

et al., 2014; Michaels et al., 2015; Šarić et al., 2016). Moreover, a key step in the conversion process is the association of soluble Aβ monomers with the fibril surface (Šarić et al., 2016). Because of the growing evidence that oligomers rather than either monomers or fibrillar aggregates are the actual culprits of Aβ toxicity, the interaction between Aβ monomers and the fibril surface is an appealing target for inhibition (Lesne et al., 2006; Munke et al., 2017).

Screening-based approaches have been employed to identify several small molecules and antibodies that abolish the formation of oligomers by specifically impeding binding between the Aβ monomer and its fibril surface (Habchi et al., 2017; Munke et al., 2017). However, because the binding interface between Aβ monomers has not been identified, using a structure-based rational design of PPI inhibitors of this type remains difficult. This gap in knowledge may critically slow or even stop efforts to find more potent candidates.

Given this continued impasse, we sought to apply a structure-based approach to derive potent inhibitors that specifically affect the interaction between soluble Aβ40 monomers and the surface of fibrillar aggregates. In our previous study, using multiscale molecular dynamic simulations, we have identified a binding interface between Aβ monomers and the fibril surface (Jiang et al., 2018a, 2018b). In particular, a helical motif in the N-terminus of Aβ monomers was found to be essential for the recognition of side-chain arrays on fibril surfaces. Interestingly, helical segments are the most frequently observed binding epitopes at PPI interfaces (Bullock et al., 2011) and are often used as sound starting points in the process of structure-based inhibitor design (Azzarito et al., 2013; Bullock et al., 2011). As such, it was compelling to investigate if a similar strategy could be extended to the discovery of inhibitors for Aβ-fibril interactions.

In practice, peptide fragments seldom exhibit favorable biological activity, which might be ascribed to their poor conformational stability. α-Helical stabilized peptides have been considered as a viable strategy with improved biophysical properties, which are capable of targeting aberrant PPIs (Mahon and Arora, 2012; Verdine and Walensky, 2007; Walensky and Bird, 2014). Given this, we recently developed a facile, helix-nucleating template (termed the Terminal Aspartic acid [TD] strategy) to restrict peptides to a helical conformation, thereby preserving their biological activity (Zhao et al., 2016). The TD strategy has a unique feature of conserving a modifiable NH_2 group on the tether for further modification. We have successfully applied this strategy to estrogen receptor α (ER-α) and solved the co-crystal structure of our TD helical peptide in complex with ER-α (Jiang et al., 2018b; Xie et al., 2017).

In this study, we combine chemical synthesis, biophysical characterization, and computational modeling to rationally design a peptide-based inhibitor that can impede the surface-catalyzed oligomerization of Aβ40. The peptide inhibitor was initially constructed based on the previous knowledge of the Aβ-fibril binding interface and subsequently improved by employing our TD strategy. The optimized inhibitor, named cyclic helical amyloid surface inhibitor-1 (cHASI-1), displays micromolar binding affinity for the fibril surface. It selectively impedes the binding between monomers and fibrils of Aβ40, interferes with surface-catalyzed Aβ40 oligomerization, and lowers the cytotoxicity of Aβ40. Our work further suggests that the inhibitor acts by recognizing side-chain array arrangement on the fibril surface. As this structural feature also exists in many other amyloid fibrils, the helical peptide scaffold discovered here may be a useful motif for the design of other amyloid-surface inhibitors.

RESULTS

Design and Optimization of the Peptide Inhibitor cHASI-1

We previously showed that the monomeric Aβ40 binding site on the Aβ fibrils comprise four adjacent side-chain arrays that belong to K_{16}, V_{18}, F_{20}, and E_{22} (Figure 1A) (Jiang et al., 2018a, 2018b). When segment $Aβ_{3-14}$ (-E_3FRHDSGYEVHH$_{14}$-) (Figure S8) of an Aβ40 monomer folds into a helix, it can use its three helical faces to interact specifically with these four side-chain arrays. The helical face including residues D_7 and E_{11} carries two acidic side chains, whereas another face including residues R_5 harbors a basic side chain. These helical surfaces attract the positively charged K_{16} and negatively charged E_{22} arrays, respectively. A third surface including residues F_4 and S_8 has a hydrophobic side chain and contacts the V_{18} and F_{20} arrays.

Based on these observations, we derived the following peptide sequence from $Aβ_{3-14}$ called helical amyloid surface inhibitor 1 (HASI-1): A_3FRADVRAERAE$_{14}$ (Figures 1B, top, S8). Compared with its parent peptide $Aβ_{3-14}$, HASI-1 carries three like charges on each of its charged helical faces and two hydrophobic side chains on its
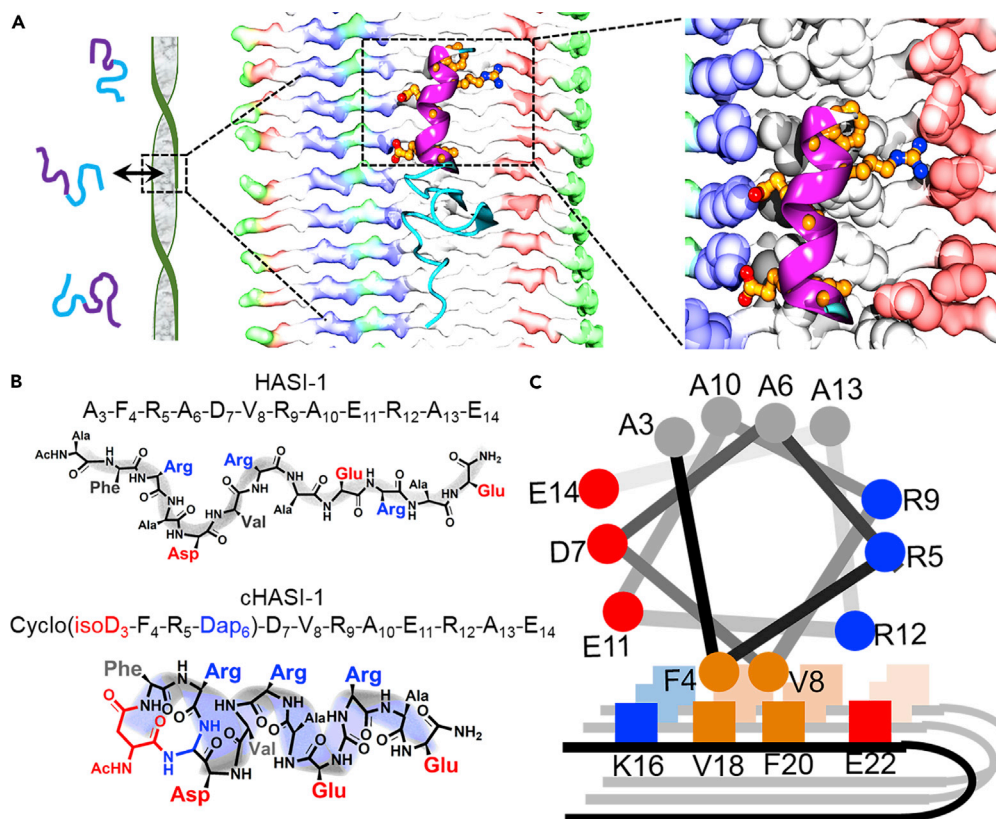
Figure 1. Design and Optimization of the Peptide Inhibitor cHASI-1

(A) Representative binding mode of Aβ40 monomer on Aβ40 fibril surface (Jiang et al., 2018a, 2018b). Aβ$_{3-14}$ is shown in purple, whereas Aβ$_{15-40}$ is shown in cyan. In the right panel, shown as blue, white and red spheres are side-chain atoms of K$_{16}$, V$_{18}$/F$_{20}$, and E$_{22}$ on the fibril surface, respectively.

(B) Scheme of HASI-1 (top) and cHASI-1 (bottom). isoD: L-isoaspartic acid; Dap: 2, 3-diaminopropionic acid.

(C) Scheme of expected binding mode of HASI-1, shown as a helical wheel, on Aβ40 fibril surface.

hydrophobic helical face (Figures 1A and 1C). In addition, we replaced the amino acids of Aβ$_{3-14}$ that are not directly involved in the binding interface at positions E$_3$, H$_6$, Y$_{10}$, and H$_{13}$ with helix-prone alanine. This should allow HASI-1 to bind more strongly to the fibril surface than the parent peptide Aβ$_{3-14}$.

To test the binding strength of HASI-1 with the fibril surface, we synthesized both Aβ$_{3-14}$ and HASI-1. We used both fluorescence polarization (FP) and isothermal titration calorimetry (ITC) experiments to measure the affinity of these peptides for Aβ40 aggregates. With a fibril-containing solution of Aβ40, the apparent K_d values for HASI-1 are ~25 μM using FP and ~20 μM using ITC. This agreement between the FP and ITC results suggests the robustness of our affinity measurement. There was no obvious binding for Aβ$_{3-14}$ (Figures 2A and S1O). Thus, and in accordance with our hypothesis, HASI-1 binds to the fibrils more strongly than its parent peptide Aβ$_{3-14}$. To confirm this finding, we also conducted equilibrium simulations of the binding between both peptides and the surface of Aβ fibrils (see Transparent Methods). We performed simulations using the same multiscale model used previously to probe the binding between the Aβ monomer and its fibril surface (Han and Schulten, 2012, 2013; Jiang et al., 2018a, 2018b). The affinities of HASI-1 and Aβ$_{3-14}$ were 4.7 μM (Table 1) and 223.2 μM at room temperature (Figures S1A and S1B), respectively. These results corroborated our experiments, indicating that HASI-1 has a much stronger affinity for Aβ fibrils than that of Aβ$_{3-14}$.

To test if the enhanced binding affinity was simply caused by the changed peptide amino acid composition, we synthesized a sequence-scrambled variant (sHASI-1, Table S1, Figure S8). This scrambled peptide had no measurable binding affinity for Aβ40 fibrils (Figures 2A and S1M). This finding confirms that the amino acid sequence in HASI-1 is critical for this peptide to bind its target.
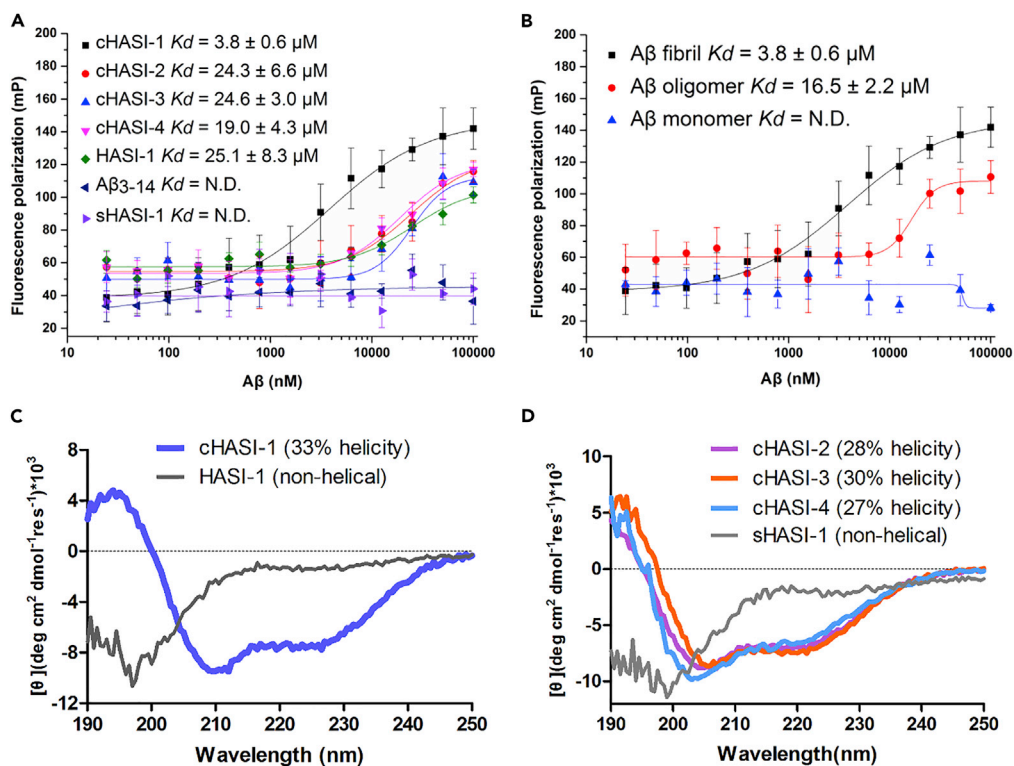
Figure 2. Binding Affinity between Peptide Inhibitors and Different Aβ40 Species, and CD Spectra of Peptide Inhibitors

(A) Fluorescence polarization assay showing binding affinity of the 20 nM fluorescein isothiocyanate-labeled peptides to 100 μM fibril-containing solution of Aβ40.

(B) Fluorescence polarization assay showing binding affinity of the 20 nM FITC-labeled cHASI-1 to Aβ40 (100 μM) in different aggregation states (freshly prepared Aβ monomers, 1 h incubated Aβ oligomers, and 24 h incubated Aβ mature fibrils) to obtain binding curves. Buffer: 20 mM sodium phosphate buffer (pH 7.4) supplemented with 200 μM EDTA and 0.02% NaN_3. Error bars represent standard deviation from the mean of three independent experiments.

(C) CD spectra of HASI-1 and cHASI-1.

(D) CD spectra of cHASIs and sHASI-1.

All CD measurements were performed in ddH_2O, pH 7.0, at 298 K. Their percent helicities were calculated by the $[\theta]_{222}$ value.

See also Figures S1–S3.

Although the ability of HASI-1 to recognize the fibril surface was significantly greater than that of Aβ$_{3-14}$, its affinity for the fibril surface is still weaker than that of full-length Aβ40 (25.1 or 20.4 μM versus 6 μM, respectively)(Meisl et al., 2014). As a helical structure may be required for the binding, it is reasonable to hypothesize that stabilizing the helical propensity of the peptide would further enhance the interaction between the peptide and the fibril surface. To this end, we adopted our TD stapling peptide strategy and mutated A_3 and A_6 of HASI-1 into an iso-D (L-isoaspartic acid) and a Dap (2,3-diaminopropionic acid), respectively. We then cross-linked the two unnatural amino acids (Figure 3), yielding a cyclic variant (cHASI-1) of HASI-1 that has a TD linker at the N terminus (Figures 1B bottom, Table 1, S8). Our previous work has shown that this N-terminal linker acts as a helical constraint by reducing the entropic cost of helix formation (Zhao et al., 2016).

Circular dichroism (CD) spectroscopy measurements showed that, in solution, cHASI-1 (33% helical content) was more helical than HASI-1 (Figure 2C). FP and ITC experiments (Figures 2A, S2H, and S2I) revealed an affinity of cHASI-1 for the Aβ fibril of 3.8 and 2.9 μM, respectively. This is approximately 6–8 times stronger than that of HASI-1 and almost two times stronger than that of full-length Aβ40 (~6 μM) (Meisl et al., 2014). Collectively, these findings indicate that cHASI-1 is a promising candidate for the inhibition of Aβ40 aggregation.

Name	Sequence	Binding Affinity		
		Experimental (μM)		Simulation (μM)
		FP	ITC	
cHASI-1	cyclo(isoD-F-R-Dap)-D-V-R-A-E-R-A-E	3.8	2.9	0.7
cHASI-2	cyclo(isoD-F-E-Dap)-D-V-R-A-R-R-A-E	24.3	27.3	24.0
cHASI-3	cyclo(isoD-F-D-Dap)-R-V-R-A-E-R-A-E	24.6	25.1	22.0
cHASI-4	cyclo(isoD-F-R-Dap)-D-V-R-A-R-E-A-E	19.0	18.9	9.6
HASI-1	A-F-R-A-D-V-R-A-E-R-A-E	25.1	20.4	4.7

Table 1. The Experimental and Simulated Affinities of cHASI-1 and Its Variants for Aβ40 Fibrils at Room Temperature

See also Figure S8.

Of note, the fitting of the ITC data could also allow us to obtain the binding stoichiometry of macromolecule-ligand interactions. Here, we obtained a binding stoichiometry of around one, which means that each cHASI-1 on average interacted with a single Aβ40 chain unit in the fibrils. According to the computational binding mode, cHASI-1 bound with fibrils could simultaneously interact with about three Aβ chains (Figure 4C). We could not reconcile this discrepancy since the exact concentration of fibrillar species could not be determined because of the stochastic nature of fibril formation. As such, all the fitting was conducted based on total Aβ40 monomer concentration, and therefore, the stoichiometry could not be established accurately. Nonetheless, as will be shown later, we were able to provide other evidence in support of the proposed binding mode (Figure 1C).

Binding Modes between cHASI-1 and Aβ40 Fibrils

Owing to the heterogeneity of the fibril-containing solution, we could not rule out that the peptide could also recognize monomeric and/or oligomeric species. To better determine the binding partners, we used freshly prepared Aβ40 solution to examine the interaction between the peptide and Aβ40 monomers. Our size exclusion chromatograms showed that only Aβ40 monomers are present in the fresh solution (Scheme S1C). FP failed to detect any obvious binding between cHASI-1 and the Aβ40 monomers (Figure 2B). Hence, cHASI-1 is unlikely to associate with monomeric species. Following Luo et al. (Wallin et al., 2018), we also prepared a sample that should contain mainly Aβ40 oligomeric species. Our transmission electron microscopy (TEM) experiment showed that the sample contained larger spherical aggregates with diameter of 15–100 nm, consistent with what was observed previously (Chimon et al., 2007), whereas our western blot experiment showed that the sample contained also small oligomers ranging from dimers to 16-mers (Figures S2A and S2B). The apparent affinity obtained with this sample is 16.5 μM (Figure 2B). Thus, cHASI-1 exhibits a moderate affinity for Aβ40 oligomers but binds much more strongly to the fibrils. We conclude that cHASI-1 specifically recognizes Aβ40 fibrils.

To locate the cHASI-1 binding sites, we also used a method based on aggregation-induced emission (AIE) (Hong et al., 2012). We used a tetra-phenylethene (TPE) group that is useful for *in situ* monitoring of amyloid fibrillation (Hong et al., 2012). We attached the TPE to the reserved N-terminal on-tether NH_2 of cHASI-1 to avoid any large structural perturbation (Figure 3). The modified peptides (cHASI-1-TPE) alone did not emit luminescence (Figures 5A–5C) owing to the multiple ionic side chains of cHASI-1, which provide excellent solubility. In contrast, we detected luminescence increase in a dose-dependent manner when cHASI-1-TPE was incubated with the fibril-containing solution, corroborating the strong ability of cHASI-1 to bind to Aβ fibrils. As expected, sHASI-1-TPE that binds weakly to the fibrils showed negligible luminescence (Figure 5D). We collected the samples from the cHASI-1-TPE/Aβ40 fibril incubation system and could clearly observe that the Aβ40 fibrils were saturated with cHASI-1-TPE (Figures 5E and 5F), suggesting that cHASI-1 is primarily absorbed on the fibril surface.

We further probed the structural details of the binding interface between cHASI-1 and the fibril surface to test if the inhibitor worked as designed. We first simulated the binding between cHASI-1 and the fibrils (see Transparent Methods). The simulated binding affinity results agreed well with the experimental value
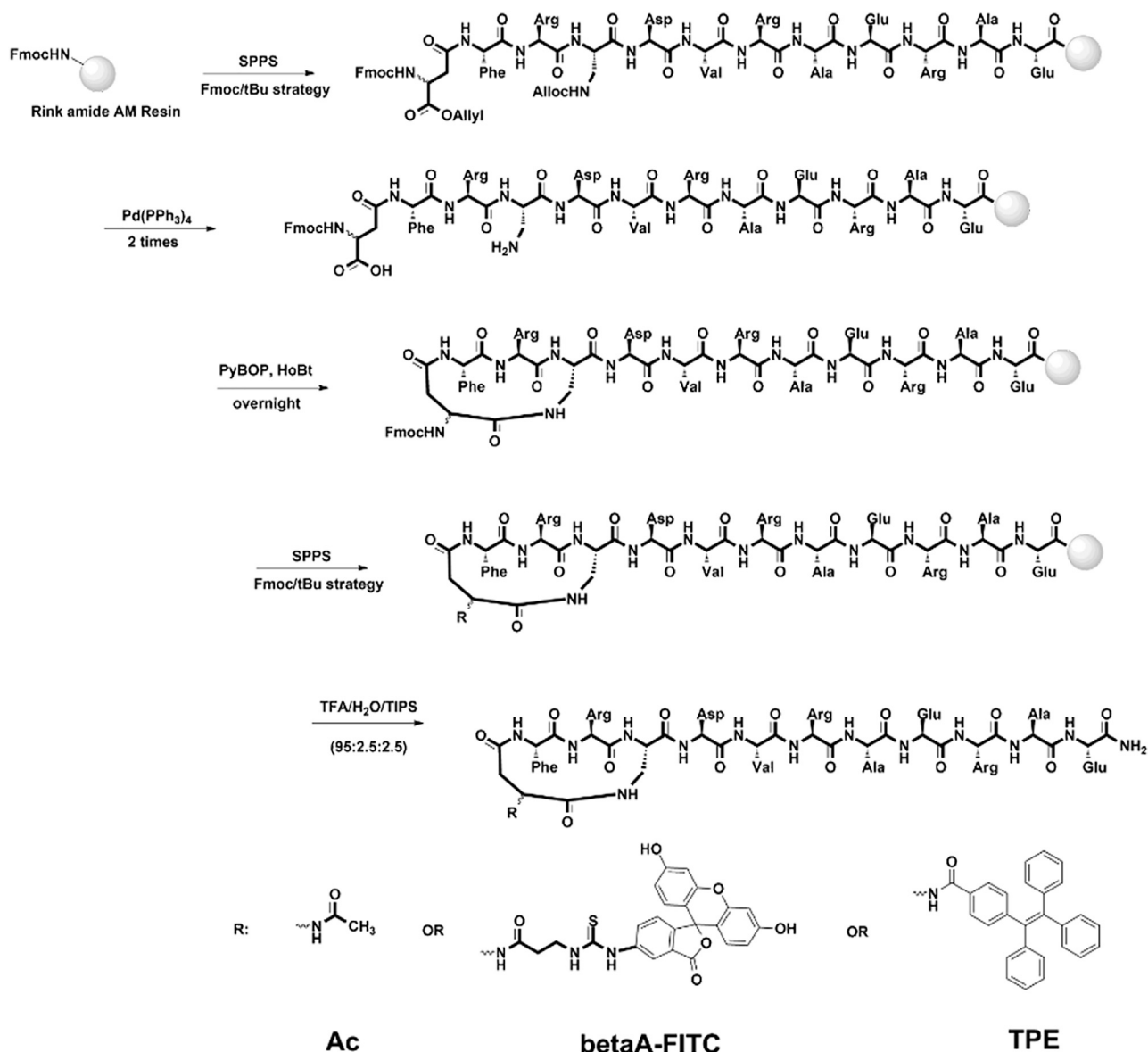
Figure 3. Representative Example for Synthesis of Stabilized Peptides cHASI-1
Synthetic details could be seen in the Transparent Methods.

(0.7 μM versus 3.8 or 2.9 μM, respectively) (Table 1 and Figure S1C). The observed interface between cHASI-1 and the fibril surface is similar to what was seen in our previous computational study of Aβ-fibril binding (Jiang et al., 2018a, 2018b). The positively charged helical face of the inhibitor was in contact with the E_{22} array of the fibril surface, whereas the negatively charged helical face of the inhibitor was in contact with the K_{16} array.

To confirm the simulation results, we synthesized a series of cHASI-1 variants (Table 1, Figure S8). Each variant swapped a distinct pair of charged residues from the two oppositely charged helical faces of cHASI-1 (cHASI-2 to cHASI-4). As our CD experiments showed that these variants have a similar helicity to cHASI-1 (Figure 2D), any change in the binding affinity should arise largely from the impact of the modifications on direct binding. If the binding pattern hypothesis is correct, any of the modifications would cause an electrostatic mismatch and impede binding. In support of our hypothesis, both FP and ITC measurements showed that all tested variants had significantly reduced (by about 5- to 6-fold) affinities for the
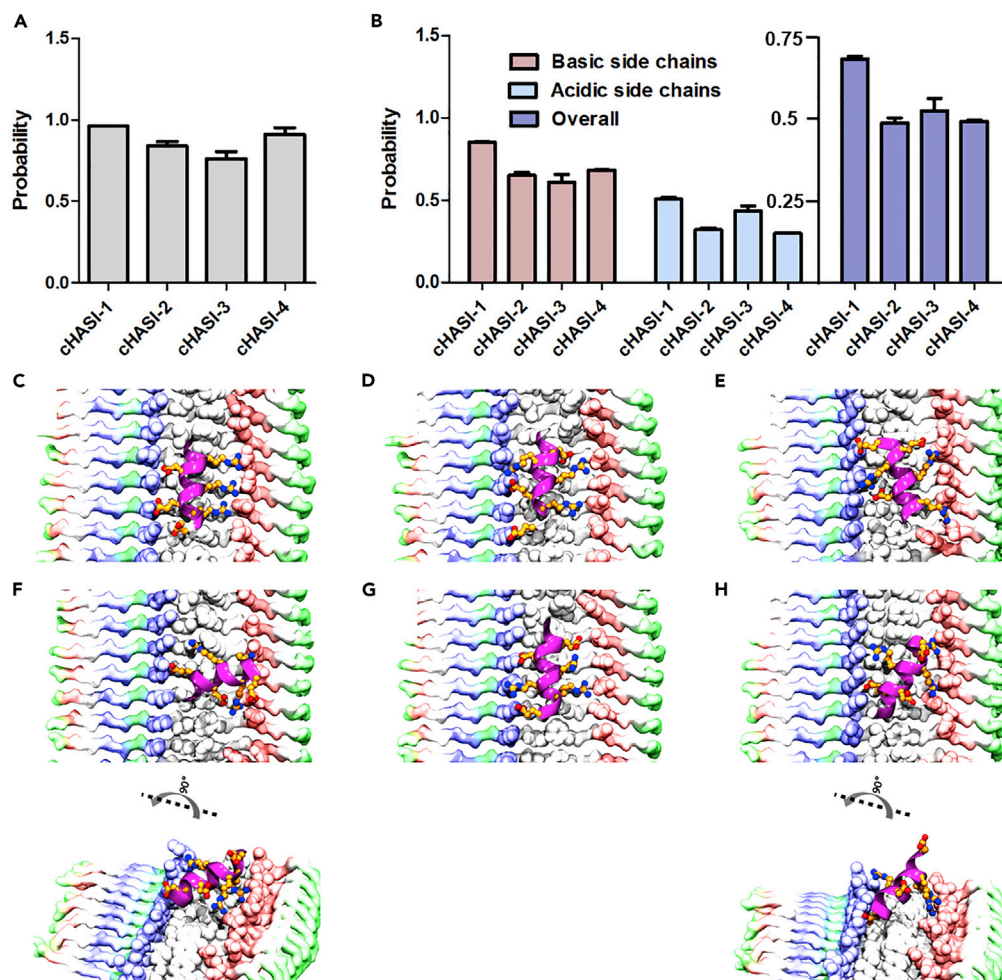
Figure 4. Probability of cHASIs Bound on Aβ40 Fibril Surface and Their Salt Bridge Interactions

(A) Probability of cHASIs (1–4) being bound on region 16–24 of Aβ40 fibril surface.

(B) Average chance of acidic and basic side chains forming salt bridge interactions with the fibril surface in bound cHASIs (1–4). A salt bridge forms if the distance between the carboxyl oxygen and ammonium/guanidinium nitrogen is shorter than 0.65 nm. Data are represented as mean ± SEM.

(C–H) Most populated binding poses of (C) cHASI-1, (D) cHASI-3, (E) cHASI-4, and (F–H) cHASI-2 on Aβ40 fibril surface. Each pose was taken as the center structure of the most populated conformation cluster. All the variants share a very similar binding pose except for cHASI-2, which exhibits also two additional binding poses with a significant probability that are no longer aligned in the direction of fibril axis (F and H).

See also Figure S7.

fibril surface as compared with cHASI-1 (Figure 2A and Table 1). Moreover, we also performed binding simulations for the variants revealing a large reduction in affinity for the fibril surface (Table 1 and Figures S1D–S1F). Structural analysis indicated that, although the binding poses of the variants remain basically unchanged (Figures 4A and 4D–H, Table S2, S7), both of their acidic and basic faces form fewer salt bridge contacts with the fibril surface than cHASI-1 (Figure 4B).

In addition, we also determined the significance of hydrophobic interaction between cHASI-1 and the fibril. In our proposed binding mode, the side chains of Phe4 and Val8 of cHASI-1 could interact with the side chains of Phe and Val on the Aβ40 fibril surface through hydrophobic interactions. Consequently, we mutated either Phe4 or Val8 of cHASI-1, or both, into alanine (Figure S8). The FP assay was used to measure their affinity for fibrils. Compared with that of cHASI-1, the fibril affinity of the two variants with single mutation (~5.4 μM for F4A and ~6.9 μM for V8A) was reduced by half. The affinity (~12.9 μM) of the variant containing double mutations (F4A/V8A) became around one-fourth of that of cHASI-1 (Figure S3). These results suggested the importance of Phe4
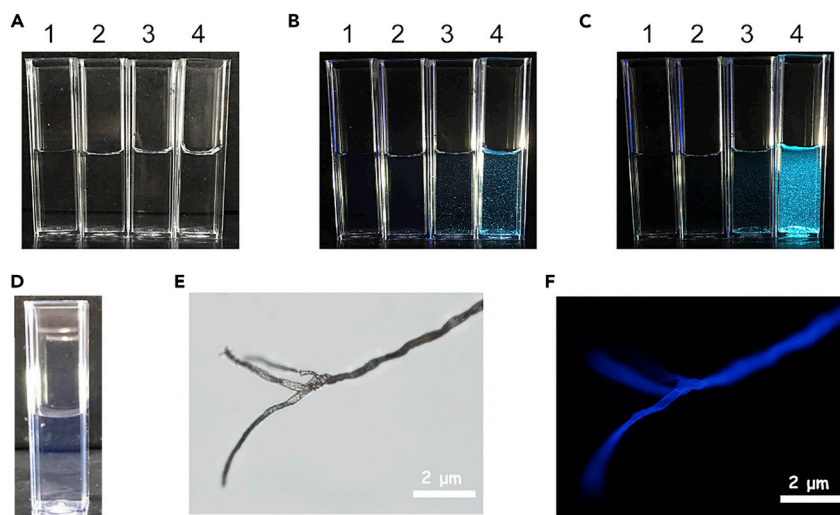
Figure 5. Photograph of cHASI-1-TPE, HASI-1-TPE, and sHASI-1-TPE under Illumination

(A–C) Photographs of 10 μM Aβ40 fibril systems incubated with 0 μM (A), 5 μM (B), and 10 μM (C) cHASI-1-TPE or sHASI-TPE, taken under illumination with a UV light of 365nm. In each panel, cuvettes 1 and 2 contained the blank buffer and 10 μM cHASI-1-TPE alone, respectively. Cuvettes 3 and 4 contained Aβ40 fibril solution incubated with HASI-TPE and cHASI-1-TPE, respectively.

(D–F) (D) Photograph of 10 μM sHASI-1-TPE taken under illumination with a UV light of 365 nm. Bright field (E) and fluorescence image (F) of 10 μM Aβ40 fibrils stained by 10 μM cHASI-1-TPE.

and Val8 for the hydrophobic interactions involved in the binding between cHASI-1 and Aβ40 fibrils, which further supported our proposed binding mode between cHASI-1 and Aβ40 fibrils.

cHASI-1 Specifically Affects Fibril-Surface-Mediated Nucleation of Aβ40

We next examined how cHASI-1 affects Aβ40 aggregation using a thioflavin T (ThT) assay to examine the aggregation kinetics in the presence or absence of varying cHASI-1 concentrations (Wolfe et al., 2010). Following Meisl et al. (2016), we initially filtered the Aβ40 monomer solution by size-exclusion chromatography (see Scheme S1C). This was done to ensure that the solution used to probe the aggregation kinetics was free of seeds (Hellstrand et al., 2010). In all cases, the aggregation kinetic curve exhibited a typical sigmoid shape, comprising an initial delay in aggregation and then a rapid formation of aggregates (Michaels et al., 2015). cHASI-1 was effective in slowing the lag phase of 10 μM Aβ40 aggregation in a dose-dependent manner from 10 to 50 μM (1 to 5 molar equivalents [M eq]) and became saturated when it reached 5 M eq (Figures 6A and S4A).

Unlike cHASI-1, HASI-1 did not cause any noticeable delay in the aggregation process unless its concentration was increased to four times of that of Aβ40 (Figure 6B). The weaker ability of HASI-1 to affect the aggregation kinetics agrees with its lower affinity for the fibril surface (Figure 2A).

The concentration of cHASI-1 needed to effectively inhibit Aβ40 aggregation is much higher than the affinity of this peptide ($K_d = 3.8$ μM). We attribute this difference to competitive binding of Aβ40 monomers. The affinity of cHASI-1 was measured when the aggregation process was almost complete. Most of the monomers would be assembled in the fibril with a low concentration (<1 μM) of free monomers left in solution (O'Nuallain et al., 2005). These free monomers would have a limited impact on the measured affinity of cHASI-1. In contrast, a much higher concentration (~10 μM) of free monomers would be present during the lag phase of the ThT kinetics experiment. Thus, many more cHASI-1 molecules are needed to compete with Aβ monomers for the fibrils. Because of this competitive binding, the inhibition effect of cHASI-1 depends on the molar ratio of the peptide inhibitor to Aβ monomers rather than the absolute amount of the peptide added. A similar conclusion was also reached previously for the inhibitory effect of other molecules on Aβ42 aggregation kinetics (Habchi et al., 2017). Nonetheless, the concentration of Aβ40 in vivo is much lower than that used in vitro (McLean et al., 1999). Thus, a lower concentration of cHASI-1 might be able to alter fibril-surface-mediated oligomerization of Aβ40 in vivo.
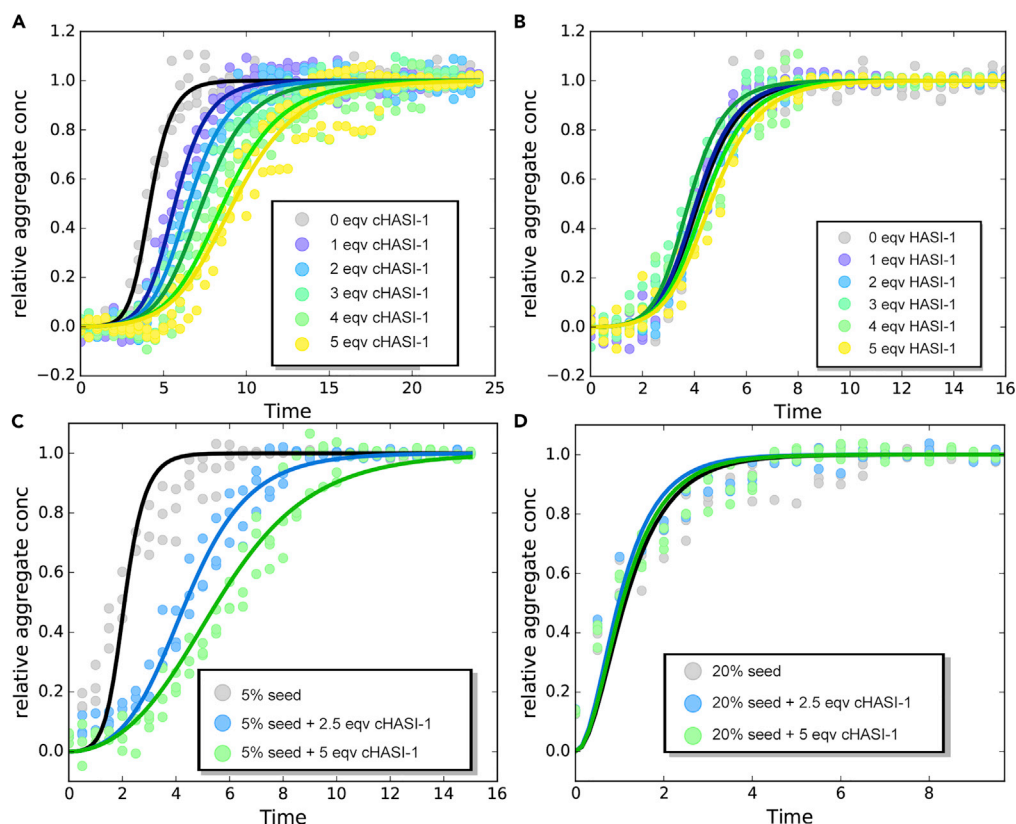
Figure 6. cHASI-1 Specifically Affects Fibril-Surface-Mediated Oligomerization of Aβ40

(A) Aggregation kinetics of 10 μM Aβ40 in the absence or presence of various amounts (10–50 μM) of cHASI-1.

(B) Kinetics of 10 μM Aβ40 aggregation in the absence or presence of 1–5 molar equivalents (10–50 μM) of HASI-1 relative to Aβ40.

(C) Aggregation kinetics of 10 μM Aβ40 upon addition of preformed Aβ40 fibrils (0.5 μM), grown in the absence or presence of 2.5 equivalent (25 μM) and 5 equivalent (50 μM) of cHASI-1.

(D) Kinetic aggregation of 10 μM Aβ40 solution in the presence of 20% of preformed seeds in the absence or presence of 2.5 or 5 equivalent of cHASI-1 (25μM or 50 μM). Buffer: 20 mM sodium phosphate buffer (pH 7.4) supplemented with 200 μM EDTA and 0.02% NaN₃, with 20 μM ThT. The data were from three independent measurements.
See also Figure S4 and Scheme S1.

The aggregation kinetics of Aβ are sensitive to several key events including nucleation in water, nucleation mediated by amyloid surface, and growth of fibrils by addition of free monomers to the ends of existing fibrils (Michaels et al., 2015). To determine which of these events are affected by cHASI-1, we conducted kinetic experiments of Aβ40 aggregation in the presence of various concentrations of seeds. The seed-containing solution was prepared through a procedure reported previously (Cukalevski et al., 2015) (see Transparent Methods). Our TEM experiment confirmed that this solution contained mainly preformed fibrillar aggregates (Figure S2C). The observed morphology was also similar to that of seeds prepared in the previous study (cf. Figure S8 in Ref. Meisl et al., 2014).

We conducted kinetic experiments of Aβ40 aggregation in the presence of various concentrations of seeds, which are mainly preformed fibrils. At low concentrations, the seeds provide additional catalytic surfaces that can allow surfaced-mediated nucleation to dominate the aggregation kinetics; at high concentrations, the kinetics of growth at fibril tips surpass those of the other events (Arosio et al., 2014a, 2014b; Cukalevski et al., 2015) Therefore, these experiments provide a means of examining the inhibitory effect of cHASI-1 on individual events of aggregation.

The low-seed-concentration and high-seed-concentration regimes for Aβ40 were shown previously to be 0.5%–10% and 10%–50%, respectively (Figures S4D and S4E) (Cukalevski et al., 2015). With the same experimental setup, we found that cHASI-1 can slow aggregation kinetics in a dose-dependent manner in the

presence of 5% preformed seeds but did not alter the aggregation kinetics in the presence of 20% pre-formed seeds (Figures 6C and 6D). This suggests that the peptide affected surface-mediated nucleation but not fibril growth.

To test if cHASI-1 could affect nucleation in water, we fit the kinetic data to the master equation (Eq. [6] in Transparent Methods) derived by Knowles that describes the rate law for the normalized mass of aggregates as a function of time (Meisl et al., 2014). The key parameters of this master equation include the rate constants of oligomerization in water (kn) or on the fibril surface ($k2$) and fibril growth ($k+$). To see if a particular microscopic event is affected by the inhibitor, we allowed the rate constant of one event to vary while fitting the data obtained at different inhibitor concentrations using single global rate constants for the other events (Habchi et al., 2017; Munke et al., 2017). Our kinetic data agreed best with a model in which cHASI-1 delays aggregation by suppressing Aβ40 nucleation on the fibril surface instead of nucleation in water (Figures 6A, S4B, and S4C).

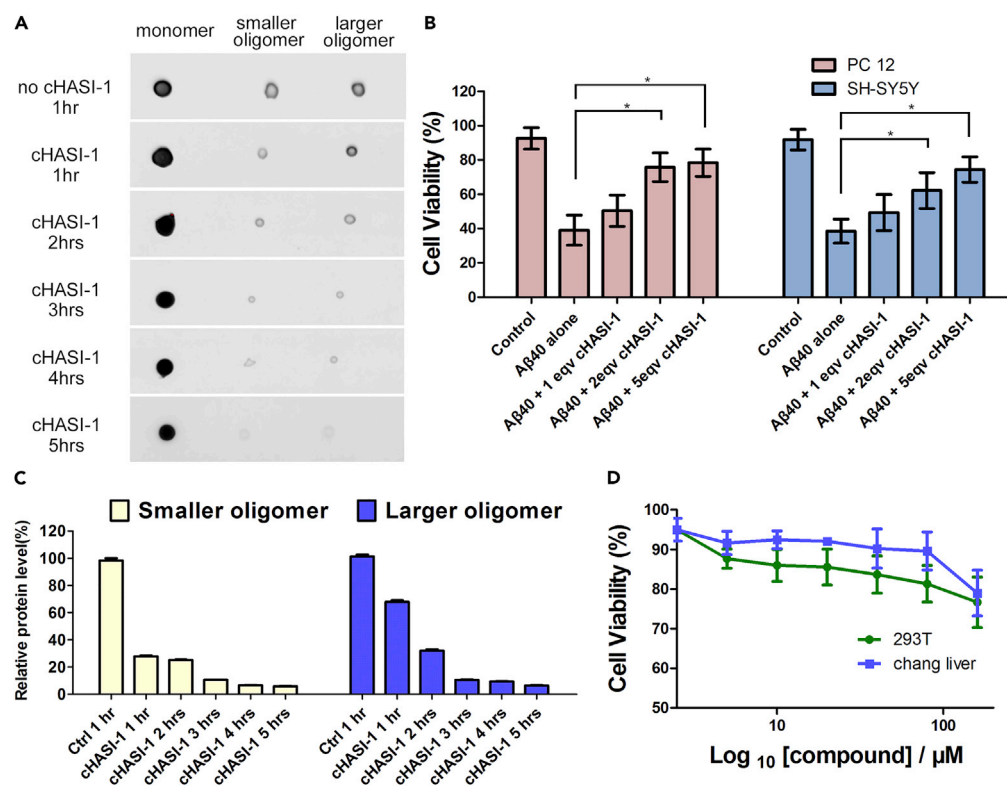### cHASI-1 Reduces Formation of Oligomers and Alleviates Aβ40 Toxicity

We monitored the amounts of monomeric and oligomeric species present in samples collected at different time points during aggregation with 5% preformed seeds. Under this condition, the surface-mediated nucleation is supposed to be dominant. Different Aβ species were separated according to molecular weight by size-exclusion chromatography (Cohen et al., 2013). All eluted fractions were divided into three groups: monomers, small oligomers (trimers to 14-mers), and larger oligomers (15-mers to 20-mers) as previously described (Cohen et al., 2015). The amounts of Aβ in each group were measured using an Aβ40-sensitive EP1876Y (Abcam) antibody quantified with Gel-Pro Analyzer (Version 4.0) software (Figure 7C).

Even at the beginning of the aggregation process, oligomer levels were decreased in the presence of cHASI-1 (Figure 7A). The amount of small and large oligomers obtained with cHASI-1 at $t = 1$ h was ~70% and ~30% less than that of the corresponding oligomer types obtained in the absence of cHASI-1 at the same time point, respectively. Moreover, the levels of small and large oligomers continued to decrease even after the lag phase was surpassed (Figure 6C). Thus, the maximum Aβ40 oligomer level was greatly reduced by cHASI-1. To further confirm that the inhibitor reduced the Aβ40 oligomer level, we also employed SDS PAGE gel electrophoresis assay to analyze the abundance of different oligomer components at the same time points described earlier. A similar reduction in oligomer level was also observed while the monomer level remained largely affected (Figure S5). Our results agreed with a study of the inhibitory effect of a chaperone protein on nucleation from the fibril surface (cf. Figure 4 in Ref. Cohen et al., 2015).

Next, we examined if cHASI-1 could also alleviate the toxicity induced by Aβ40 aggregation. PC12 and SH-SY5Y cells, which have been widely used in the studies of amyloid toxicity (Andreetto et al., 2015; Chen et al., 2017, 2018; Choi et al., 2017; Cohen et al., 2015; Nerelius et al., 2009), were employed in the present study. These two cell types were incubated with the same oligomer sample prepared as earlier (10 μM Aβ40 with 0.5 μM seeds) in the presence or the absence of cHASI-1 to assess the impact of cHASI-1 on the cyto-toxicity of Aβ40 aggregates. Cellular viability was approximately 30%–40% survival without inhibitor and was rescued to approximately 75%–85% survival with 5 M eq of cHASI-1 treatment (Figures 7B and S6A). As a control, we also examined the inhibitory effect of three documented amyloid β inhibitors, including Curcumin (Baum and Ng, 2004; Kim et al., 2001; Yang et al., 2005), Galanthamine (Matharu et al., 2009), and Cucurbit [7] uril (Lee et al., 2014). The cHASI-1 was just as effective as these inhibitors (Figure S6B).

As the oligomer sample used was a mixture of monomers, oligomers, and fibrillar seeds, we further incubated the cells with either the fresh monomer solution or the fibril sample to assess which of the species was responsible for the observed cellular toxicity. As shown in Figure S6C, Aβ40 monomers had little effect on cellular viability and Aβ40 fibrils exhibited only moderate toxicity that was still much less than that observed when the cells were incubated with the oligomer sample. Therefore, the observed cellular toxicity was mainly caused by the oligomer species in the sample, and cHASI-1 protected the cells from the aggregate toxicity most likely by lowering the oligomer level.

Finally, we tested the intrinsic cytotoxicity of cHASI-1 using two normal cell lines (HEK-293 and Chang liver) as well as the PC12 and SH-SY5Y cells used in the toxicity test. For all the cell types examined, 3-(4, 5-di-methylthiazol-2-yl)-2, 5-diphenylt-etrazolium bromide (MTT) results demonstrated only a slight effect on

Figure 7. cHASI-1 Reduces Formation of Oligomers and Alleviates Aβ40 Toxicity

(A) Amounts of Aβ40 oligomers in the absence or presence of cHASI-1. Monomers and oligomers were separated with size-exclusion chromatography and quantified with the EP1876Y (Abcam) antibody at t = 1, 2, 3, 4, and 5 h. Initial concentration of Aβ40 monomers and cHASI-1 were 10 μM and 50 μM, respectively. Preformed fibrils (0.5 μM) were added to promote the oligomerization.

(B) Viability of PC12 and SH-SY5Y treated with preformed Aβ40 fibrils (0.5 μM) and fresh monomer (10 μM) in the absence or presence of 10, 20, and 50 μM cHASI-1. The average and standard deviations shown are over four replicates of each condition. *, $p < 0.05$, one-way analysis of variance.

(C) Dot-blot assay was quantified by the use of Gel-Pro Analyzer (version 4.0) software. The average and standard deviations shown are over three times of measurements.

(D) Viability of two types of normal cells treated with 2.5–160 μM cHASI-1. Error bars represent SEMs of at least three independent measurements.

See also Figures S5 and S6.

normal cellular growth and proliferation even with the addition of over 100 μM cHASI-1 (Figures 7D and S6D). This finding highlights the low cytotoxicity of cHASI-1, making it a promising candidate for inhibition of Aβ aggregation.

It should be noted that, despite the numerous studies of surface-mediated nucleation of Aβ40, it is not yet clear whether the oligomers produced on the fibril surface are all nuclei. The results presented earlier revealed that the cHASI-1 could reduce the level of nuclei formed on the fibril surface, but we could not rule out the possibility that the formation of certain types of oligomers on the fibril surface may not be affected by the inhibitor. Nevertheless, if such oligomers existed, their cellular toxicity should be insignificant, which would otherwise contradict to what was observed in our cellular toxicity assays.

DISCUSSION

We have rationally designed a peptide-based inhibitor of Aβ aggregation based on structural insights revealed by our previous computational study of the binding between Aβ and fibrils (Jiang et al., 2018a, 2018b). We demonstrated that the inhibitor, when constrained to a helical conformation, selectively impedes the binding of Aβ monomers to the lateral surface of Aβ fibrils, suppressing Aβ fibril-surface-mediated oligomerization.

Furthermore, we showed that, owing to its ability to reduce the production of oligomers, our helical peptide inhibitor mitigates the cellular toxicity of Aβ40.

Owing to the lack of apparent pockets, fibril surfaces have been targeted mainly by flat molecules (Jiang et al., 2013; Young et al., 2017). Our study demonstrates that a helical peptide scaffold can also recognize the fibril surface. In a helical conformation, peptides with proper sequences can arrange their amino acid side chains with similar properties on the same helical face. When aligned in the direction of the fibril, the inhibitor uses its helical face to form extensive interactions with side-chain arrays on the fibril surface. Several faces of the helix of the designed inhibitor, cHASI-1, simultaneously interact with adjacent side-chain arrays on the Aβ40 fibril surface, maximizing both hydrophobic and electrostatic attraction. Since side-chain arrays are a common feature of many other amyloid fibrils of alpha-synuclein, human islet amyloid polypeptide, and prions (Ke et al., 2017), this helical peptide scaffold can be applied to the development of modulators of other protein aggregation.

Artificially mimicking conformationally specific peptides by chemically "stapling" amino acids at the primary sequence level has become increasingly attractive (Walensky and Bird, 2014). Owing to their facile modification, it is feasible to construct specific peptides in a particular conformation by a series of strategies, such as introducing β-amino acids (Schmitt et al., 2006). In this study, helicity is subtly influenced by the N-terminal nucleating TD tether as shown by CD (Figures 2C and 2D). Different from most nucleating methods, our TD strategy preserves an NH_2 group at the N terminus, providing an access point for additional chemical modifications. Various functional groups may be stitched, including the AIE dye used here and others such as black phosphorus (Chen et al., 2018) for nano-medicine. We anticipate that our combined experimental and computational approach will allow for well-designed and powerful peptides for better understanding and therapeutic management of amyloid diseases.

Limitation of Study

This work reports an important discovery of recognition patterns of Aβ fibril surface with conformation constraint peptides, which may offer a general concept for designing modulators for amyloid-β aggregation by peptides. Although we have demonstrated the pattern experimentally *in vitro*, the *in vivo* performance remains to be answered. To improve the *in vivo* performance, we could further manipulate the chemical structure of cHASI-1. For example, we could sew a shuttle peptide at the N terminus of cHASI-1 to address the delivery issue across the blood-brain barrier (Oller Salvia et al., 2016).

METHODS

All methods can be found in the accompanying Transparent Methods supplemental file.

SUPPLEMENTAL INFORMATION

Supplemental Information can be found online at https://doi.org/10.1016/j.isci.2019.06.022.

AUTHOR CONTRIBUTIONS

Conceptualization and design – Y.J., X.J., W.H., Z.L. Data generation – Y.J., X.J., X.S., F. Yang, Y.C., X.Q., Z.H., M.X., N.L., Q.F.). Data analysis and interpretation – Y.J., X.J., W.H., Z.L. Manuscript preparation – Y.J., X.J., F. Yin, W.H., Z.L. Review and editing – F. Yin, W.H., Z.L. Funding acquisition – F. Yin, W.H., Z.L.

DECLARATION OF INTERESTS

The authors declare no competing interests.

iScience

REFERENCES

Andreetto, E., Malideli, E., Yan, L.M., Kracklauer, M., Farbiarz, K., Tatarek Nossol, M., Rammes, G., Prade, E., Neumüller, T., and Caporale, A. (2015). A hot-segment-based approach for the design of cross-amyloid interaction surface mimics as inhibitors of amyloid self-assembly. Angew. Chem. Int. Ed. *54*, 13095–13100.

Arosio, P., Cukalevski, R., Frohm, B., Knowles, T.P.J., and Linse, S. (2014a). Quantification of the concentration of Aβ42 propagons during the lag phase by an amyloid chain reaction assay. J. Am. Chem. Soc. *136*, 219–225.

Arosio, P., Vendruscolo, M., Dobson, C.M., and Knowles, T.P.J. (2014b). Chemical kinetics for drug discovery to combat protein aggregation diseases. Trends. Pharmacol. Sci. *35*, 127–135.

Azzarito, V., Long, K., Murphy, N.S., and Wilson, A.J. (2013). Inhibition of α-helix-mediated protein-protein interactions using designed molecules. Nat. Chem. *5*, 161–173.

Bartolini, M., and Andrisano, V. (2010). Strategies for the inhibition of protein aggregation in human diseases. ChemBioChem *11*, 1018–1035.

Baum, L., and Ng, A. (2004). Curcumin interaction with copper and iron suggests one possible mechanism of action in Alzheimer's disease animal models. J. Alzheimers Dis. *6*, 367–377.

Bullock, B.N., Jochim, A.L., and Arora, P.S. (2011). Assessing helical protein interfaces for inhibitor design. J. Am. Chem. Soc. *133*, 14220–14223.

Chen, D., Qin, W., Wen, G., Shi, B., Liu, Z., Wang, Y., Zhou, Q., Quan, J., Zhou, B., and Bu, X. (2017). Dissociation of haemolytic and oligomer-preventing activities of gramicidin S derivatives targeting the amyloid-β N-terminus. Chem. Commun. (Camb.) *53*, 13340–13343.

Chen, W., Ouyang, J., Yi, X., Xu, Y., Niu, C., Zhang, W., Wang, L., Sheng, J., Deng, L., Liu, Y.N., and Guo, S. (2018). Black phosphorus nanosheets as a neuroprotective nanomedicine for neurodegenerative disorder therapy. Adv. Mater. *30*, 1703458.

Chimon, S., Shaibat, M.A., Jones, C.R., Calero, D.C., Aizezi, B., and Ishii, Y. (2007). Evidence of fibril-like β-sheet structures in a neurotoxic amyloid intermediate of Alzheimer's β-amyloid. Nat. Struct. Mol. Biol. *14*, 1157.

Chiti, F., and Dobson, C.M. (2006). Protein misfolding, functional amyloid, and human disease. Annu. Rev. Biochem. *75*, 333–366.

Choi, T.S., Lee, H.J., Han, J.Y., Lim, M.H., and Kim, H.I. (2017). Molecular insights into human serum albumin as a receptor of amyloid-β in the extracellular region. J. Am. Chem. Soc. *139*, 15437–15445.

Cohen, S.I.A., Arosio, P., Presto, J., Kurudenkandy, F.R., Biverstal, H., Dolfe, L.,

Dunning, C., Yang, X., Frohm, B., Vendruscolo, M., et al. (2015). A molecular chaperone breaks the catalytic cycle that generates toxic Aβ oligomers. Nat. Struct. Mol. Biol. *22*, 207–213.

Cohen, S.I., Linse, S., Luheshi, L.M., Hellstrand, E., White, D.A., Rajah, L., Otzen, D.E., Vendruscolo, M., Dobson, C.M., and Knowles, T.P.J. (2013). Proliferation of amyloid-β42 aggregates occurs through a secondary nucleation mechanism. Proc. Natl. Acad. Sci. U S A *110*, 9758–9763.

Cukalevski, R., Yang, X., Meisl, G., Weininger, U., Bernfur, K., Frohm, B., Knowles, T.P.J., and Linse, S. (2015). The Aβ40 and Aβ42 peptides self-assemble into separate homomolecular fibrils in binary mixtures but cross-react during primary nucleation. Chem. Sci. *6*, 4215–4233.

Doig, A.J., and Derreumaux, P. (2015). Inhibition of protein aggregation and amyloid formation by small molecules. Curr. Opin. Struc. Biol. *30*, 50–56.

Goyal, D., Shuaib, S., Mann, S., and Goyal, B. (2017). Rationally designed peptides and peptidomimetics as inhibitors of amyloid-β (Aβ) aggregation: potential therapeutics of Alzheimer's disease. ACS Comb. Sci. *19*, 55–80.

Habchi, J., Chia, S., Limbocker, R., Mannini, B., Ahn, M., Perni, M., Hansson, O., Arosio, P., Kumita, J.R., Challa, P.K., et al. (2017). Systematic development of small molecules to inhibit specific microscopic steps of Aβ42 aggregation in Alzheimer's disease. Proc. Natl. Acad. Sci. U S A *114*, E200–E208.

Han, W., and Schulten, K. (2012). Further optimization of a hybrid united-atom and coarse-grained force field for folding simulations: improved backbone hydration and interactions between charged side chains. J. Chem. Theory. Comput. *8*, 4413–4424.

Han, W., and Schulten, K. (2013). Characterization of folding mechanisms of Trp-cage and WW-domain by network analysis of simulations with a hybrid-resolution model. J. Phys. Chem. B *117*, 13367–13377.

Härd, T., and Lendel, C. (2012). Inhibition of amyloid formation. J. Mol. Biol. *421*, 441–465.

Hellstrand, E., Boland, B., Walsh, D.M., and Linse, S. (2010). Amyloid β-protein aggregation produces highly reproducible kinetic data and occurs by a two-phase process. ACS Chem. Neurosci. *1*, 13–18.

Hong, Y., Meng, L., Chen, S., Leung, C.W., Da, L.T., Faisal, M., Silva, D.A., Liu, J., Lam, J.W., Huang, X., and Tang, B.Z. (2012). Monitoring and inhibition of insulin fibrillation by a small organic fluorogen with aggregation-induced emission characteristics. J. Am. Chem. Soc. *134*, 1680–1689.

Jiang, L., Liu, C., Leibly, D., Landau, M., Zhao, M., Hughes, M.P., and Eisenberg, D.S. (2013). Structure-based discovery of fiber-binding compounds that reduce the cytotoxicity of amyloid beta. Elife *2*, e00857.

Jiang, X., Cao, Y., and Han, W. (2018a). In silico study of recognition between Aβ40 and Aβ40 fibril surfaces: an N-terminal helical recognition motif and its implications for inhibitor design. ACS. Chem. Neurosci. *9*, 935–944.

Jiang, Y., Deng, Q., Zhao, H., Xie, M., Chen, L., Yin, F., Qin, X., Zheng, W., Zhao, Y., and Li, Z.G. (2018b). Development of stabilized peptide-based PROTACs against estrogen receptor α. ACS. Chem. Biol. *13*, 628–635.

Ke, P.C., Sani, M.A., Ding, F., Kakinen, A., Javed, I., Separovic, F., Davis, T.P., and Mezzenga, R. (2017). Implications of peptide assemblies in amyloid diseases. Chem. Soc. Rev. *46*, 6492–6531.

Kim, D.S., Park, S., and Kim, J. (2001). Curcuminoids from *Curcuma longa* L. (Zingiberaceae) that protect PC12 rat pheochromocytoma and normal human umbilical vein endothelial cells from βA (1–42) insult. Neurosci. Lett. *303*, 57–61.

Lee, H.H., Choi, T.S., Lee, S.J.C., Lee, J.W., Park, J., Ko, Y.H., Kim, W.J., Kim, K., and Kim, H.I. (2014). Supramolecular inhibition of amyloid fibrillation by cucurbit [7] uril. Angew. Chem. Int. Ed. *53*, 7461–7465.

Lesne, S., Koh, M.T., Kotilinek, L., Kayed, R., Glabe, C.G., Yang, A., Gallagher, M., and Ashe, K.H. (2006). A specific amyloid-beta protein assembly in the brain impairs memory. Nature *440*, 352–357.

Lorenzo, A., and Yankner, B.A. (1994). Beta-amyloid neurotoxicity requires fibril formation and is inhibited by Congo red. Proc. Natl. Acad. Sci. U S A *91*, 12243–12247.

Mahon, A.B., and Arora, P.S. (2012). End-Capped α-helices as modulators of protein function. Drug Discov. Today Technol. *9*, e57–e62.

Matharu, B., Gibson, G., Parsons, R., Huckerby, T.N., Moore, S.A., Cooper, L.J., Millichamp, R., Allsop, D., and Austen, B. (2009). Galantamine inhibits β-amyloid aggregation and cytotoxicity. J. Neurol. Sci. *280*, 49–58.

McLean, C.A., Cherny, R.A., Fraser, F.W., Fuller, S.J., Smith, M.J., Beyreuther, K., Bush, A.I., and Masters, C.L. (1999). Soluble pool of Abeta amyloid as a determinant of severity of neurodegeneration in Alzheimer's disease. Ann. Neurol. *46*, 860–866.

Meisl, G., Kirkegaard, J.B., Arosio, P., Michaels, T.C., Vendruscolo, M., Dobson, C.M., Linse, S., and Knowles, T.P.J. (2016). Molecular mechanisms of protein aggregation from global fitting of kinetic models. Nat. Protoc. *11*, 252–272.

Meisl, G., Rajah, L., Cohen, S.A.I., Pfammatter, M., Šarić, A., Hellstrand, E., Buell, A.K., Aguzzi, A., Linse, S., Vendruscolo, M., et al. (2017). Scaling behaviour and rate-determining steps in filamentous self-assembly. Chem. Sci. *8*, 7087–7097.

Meisl, G., Yang, X., Hellstrand, E., Frohm, B., Kirkegaard, J.B., Cohen, S.I., Dobson, C.M., Linse, S., and Knowles, T.P.J. (2014). Differences in nucleation behavior underlie the contrasting aggregation kinetics of the Aβ40 and Aβ42 peptides. Proc. Natl. Acad. Sci. U S A *111*, 9384–9389.

Michaels, T.C., Lazell, H.W., Arosio, P., and Knowles, T.P.J. (2015). Dynamics of protein aggregation and oligomer formation governed by secondary nucleation. J. Chem. Phys. *143*, 054901.

Munke, A., Persson, J., Weiffert, T., De Genst, E., Meisl, G., Arosio, P., Carnerup, A., Dobson, C.M., Vendruscolo, M., Knowles, T.P.J., and Linse, S. (2017). Phage display and kinetic selection of antibodies that specifically inhibit amyloid self-replication. Proc. Natl. Acad. Sci. U S A *114*, 6444–6449.

Nerelius, C., Sandegren, A., Sargsyan, H., Raunak, R., Leijonmarck, H., Chatterjee, U., Fisahn, A., Imarisio, S., Lomas, D.A., Crowther, D.C., et al. (2009). Alpha-helix targeting reduces amyloid-beta peptide toxicity. Proc. Natl. Acad. Sci. U S A *106*, 9191–9196.

Oller-Salvia, B., Sánchez-Navarro, M., Ciudad, S., Guiu, M., Arranz-Gibert, P., Garcia, C., Gomis, R.R., Cecchelli, R., García, J., Gi-ralt, E., and Teixidó, M. (2016). MiniAp-4: a venom-inspired peptidomimetic for brain delivery. Angew. Chem. Int. Ed. *55*, 572–575.

O'Nuallain, B., Shivaprasad, S., Kheterpal, I., and Wetzel, R. (2005). Thermodynamics of A beta(1-40) amyloid fibril elongation. Biochemistry *44*, 12709–12718.

Šarić, A., Buell, A.K., Meisl, G., Michaels, T.C., Dobson, C.M., Linse, S., Knowles, T.P.J., and Frenkel, D. (2016). Physical determinants of the self-replication of protein fibrils. Nat. Phys. *12*, 874.

Schmitt, M.A., Choi, S.H., Guzei, I.A., and Gellman, S.H. (2006). New helical foldamers: heterogeneous backbones with 1:2 and 2:1 alpha:beta-amino acid residue patterns. J. Am. Chem. Soc. *128*, 4538–4539.

Sievers, S.A., Karanicolas, J., Chang, H.W., Zhao, A., Jiang, L., Zirafi, O., Stevens, J.T., Munch, J., Baker, D., and Eisenberg, D. (2011). Structure-based design of non-natural amino-acid inhibitors of amyloid fibril formation. Nature *475*, 96–100.

Soto, C., Sigurdsson, E.M., Morelli, L., Kumar, R.A., Castaño, E.M., and Frangione, B. (1998). Beta-sheet breaker peptides inhibit fibrillogenesis in a rat brain model of amyloidosis: implications for Alzheimer's therapy. Nat. Med. *4*, 822–826.

Tycko, R. (2011). Solid-state NMR studies of amyloid fibril structure. Annu. Rev. Phys. Chem. *62*, 279–299.

Verdine, G.L., and Walensky, L.D. (2007). The challenge of drugging undruggable targets in cancer: lessons learned from targeting BCL-2 family members. Clin. Cancer Res. *13*, 7264–7270.

Walensky, L.D., and Bird, G.H. (2014). Hydrocarbon-stapled peptides: principles, practice, and progress. J. Med. Chem. *57*, 6275–6288.

Wallin, C., Hiruma, Y., Wärmländer, S.K.T.S., Huvent, I., Jarvet, J., Abrahams, J.P., Gräslund, A., Lippens, G., and Luo, J. (2018). The neuronal tau protein blocks in vitro fibrillation of the amyloid-β (Aβ) peptide at the oligomeric stage. J. Am. Chem. Soc. *140*, 8138–8146.

Wolfe, L.S., Calabrese, M.F., Nath, A., Blaho, D.V., Miranker, A.D., and Xiong, Y. (2010). Protein-induced photophysical changes to the amyloid indicator dye thioflavin T. Proc. Natl. Acad. Sci. U S A *107*, 16863–16868.

Xie, M., Zhao, H., Liu, Q., Zhu, Y., Yin, F., Liang, Y., Jiang, Y., Wang, D., Hu, K., Qin, X., et al. (2017). Structural basis of inhibition of ERα-coactivator interaction by high-affinity N-terminus isoaspartic acid tethered helical peptides. J. Med. Chem. *60*, 8731–8740.

Yang, F., Lim, G.P., Begum, A.N., Ubeda, O.J., Simmons, M.R., Ambegaokar, S.S., Chen, P.P., Kayed, R., Glabe, C.G., and Frautschy, S.A. (2005). Curcumin inhibits formation of amyloid β oligomers and fibrils, binds plaques, and reduces amyloid in vivo. J. Biol. Chem. *280*, 5892–5901.

Young, L.M., Ashcroft, A.E., and Radford, S.E. (2017). Small molecule probes of protein aggregation. Curr. Opin. Chem. Biol. *39*, 90–99.

Zhao, H., Liu, Q.S., Geng, H., Tian, Y., Cheng, M., Jiang, Y.H., Xie, M.S., Niu, X.G., Jiang, F., Zhang, Y.O., et al. (2016). Crosslinked aspartic acids as helix-nucleating templates. Angew. Chem. Int. Ed. *55*, 12088–12093.

Supplemental Information

α-Helical Motif as Inhibitors of Toxic

Amyloid-β Oligomer Generation via Highly

Specific Recognition of Amyloid Surface

Yixiang Jiang, Xuehan Jiang, Xiaodong Shi, Fadeng Yang, Yang Cao, Xuan Qin, Zhanfeng Hou, Mingsheng Xie, Na Liu, Qi Fang, Feng Yin, Wei Han, and Zigang Li

Supporting Tables and Figures

Table S1: Peptides Characterization, Related to Table 1.

Calculated and Found m/z are presented as [M+1H] [1+] / [M/2+H] [2+] / [M/3+H] [3+]

Peptide	Sequence	Chemical Formula	Calculated m/z	Found m/z
cHASI-1	Ac-cyclo(isoD-F-R-Dap)-D-V-R-A-E-R-A-E-NH$_2$	C$_{61}$H$_{97}$N$_{23}$O$_{20}$	1471.73/735.86	492.1/737.5
cHASI-2	Ac-cyclo(isoD-F-R-Dap)-D-V-R-A-R-E-A-E-NH$_2$	C$_{62}$H$_{99}$N$_{23}$O$_{20}$	1471.73/735.86	491.7/737.0
cHASI-3	Ac-cyclo(isoD-F-E-Dap)-D-V-R-A-R-R-A-E-NH$_2$	C$_{61}$H$_{97}$N$_{23}$O$_{20}$	1471.73/735.86	491.9/737.2
cHASI-4	Ac-cyclo(isoD-F-D-Dap)-R-V-R-A-E-R-A-E-NH$_2$	C$_{61}$H$_{97}$N$_{23}$O$_{20}$	1471.73/735.86	492.0/737.4
HASI-1	Ac-A-F-R-A-D-V-R-A-E-R-A-E-NH$_2$	C$_{58}$H$_{96}$N$_{22}$O$_{18}$	1431.56/715.78	478.0/716.8
sHASI-1	Ac-F-E-A-E-R-R-V-A-A-D-R-A-NH$_2$	C$_{58}$H$_{96}$N$_{22}$O$_{18}$	1431.56/715.78	478.1/716.5
cHASI-1-TPE	TPE-cyclo(isoD-F-R-Dap)-D-V-R-A-E-R-A-E-NH$_2$	C$_{86}$H$_{113}$N$_{23}$O$_{20}$	1787.85/893.93	597.2/895.2
sHASI-1-TPE	TPE-F-E-A-E-R-R-V-A-A-D-R-A-NH$_2$	C$_{85}$H$_{114}$N$_{22}$O$_{19}$	1746.86/873.43	583.5/875.0
Aβ$_{3-14}$	Ac-E-F-R-H-D-S-G-Y-E-V-H-H-NH$_2$	C$_{68}$H$_{92}$N$_{22}$O$_{21}$	1552.68/777.34/517.6	518.85/777.60

Table S2: Parameters for cHASI-1 to cHASI-4, Related to Figure 4.

cHASI-1 and cHASI-2												
Residue ID	1	2	3	4	5	6	7	8	9	10	11	12
φ_0 (°)	66.52	-69	70.53	72.43	-56	71.57	-67.5	-73.5	-76	59.53	43.95	12.58
K (kJmol^{-1}rad^{-2})	12.16	11.77	5.8	12.5	14.27	17.76	6.47	15.57	22.66	22.56	6.29	0.8
ψ_0 (°)	12.79	-4.07	22.26	26.86	23.35	36.48	19.92	-9.7	20.49	14.89	6.25	-7.91
F (kJmol^{-1}rad^{-2})	1	1.5	4	7.7	4.89	6.96	9.35	1.68	5.7	3.88	0.57	1
cHASI-3												
Residue ID	1	2	3	4	5	6	7	8	9	10	11	12
φ_0 (°)	66.55	68.97	70.58	72.43	55.99	71.57	-67.5	73.47	-76	-59.5	43.91	12.52

K (kJmol⁻¹rad⁻²)	12.13	11.75	5.77	12.48	14.24	17.73	6.44	15.55	22.62	22.52	6.27	0.8
ψ_0 (°)	12.58	-3.97	-22.1	26.82	23.21	36.47	19.85	-9.53	20.45	14.87	6.39	-7.97
F (kJmol⁻¹rad⁻²)	1	1.5	3.97	7.67	4.85	6.93	9.3	1.67	5.7	3.85	0.57	1

cHASI-4

|												
Residue ID	66.57	-69	70.55	72.43	55.95	71.57	67.44	-73.5	-76	59.53	43.78	11.59
φ_0 (°)	12.1	11.71	5.74	12.44	14.21	17.7	6.41	15.51	22.59	22.47	6.23	0.8
K (kJmol⁻¹rad⁻²)	12.26	-4.04	22.08	-26.8	23.22	-36.5	19.74	-9.61	20.58	14.34	8.46	-7.4
ψ_0 (°)	0.95	1.5	3.94	7.64	4.83	6.9	9.24	1.67	5.7	3.76	0.51	1
F (kJmol⁻¹rad⁻²)	66.57	-69	70.55	72.43	55.95	71.57	67.44	-73.5	-76	59.53	43.78	11.59
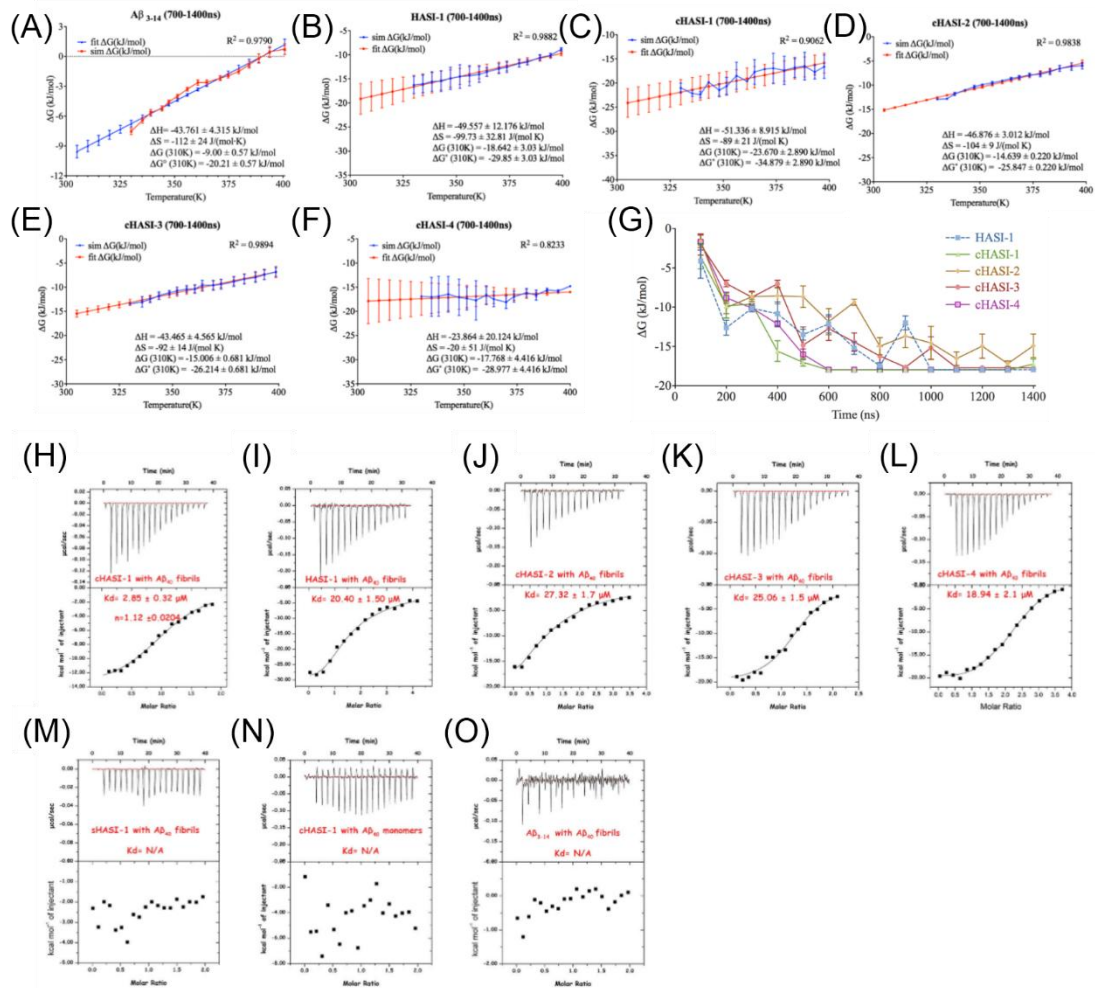
Figure S1. In-silico and experimental binding affinity between peptides and fibril surface, Related to Figure 2. (A-F) Binding affinity of peptides on fibril surface changes with temperature. Blue lines and dots represent the binding affinity calculated from simulation, while the red ones come from the linear fitting of binding affinity and temperature. Error bars is calculated by four blocks average from the 700-1400ns. (G) Time evolution of binding affinity of peptides on fibril surface. Binding affinity is calculated during each 100ns simulation. The error bar is calculated as the standard error of binding affinity for 4 blocks within the 100ns simulation. (H-O) Isothermal calorimetry titration (ITC) thermogram for the titration of a solution of 10 μM Aβ40 fibrils with (H) 100 μM cHASI-1 and with (I) 250 μM HASI-1, (J) 220 μM cHASI-2, (K) 120 μM cHASI-3, (L) 200 μM cHASI-4, (M)100 μM sHASI-1, (N) 100 μM Aβ3-14, and ITC thermogram for the titration of a solution of 10 μM Aβ40 monomers with (O) 100 μM cHASI. The upper panel represents the heat burst curves and each curve is a result of a 2 μL injection of peptide into Aβ40 fibrils solution in the sample cell. The lower panel is the corrected injection heats associated with each injection plotted as a function of the molar ratio (peptide/ Aβ40). Buffer: 20 mM sodium phosphate buffer (pH 8) supplemented with 200 μM EDTA and 0.02% NaN₃. Error bars represent standard deviation from the mean of three independent experiments.
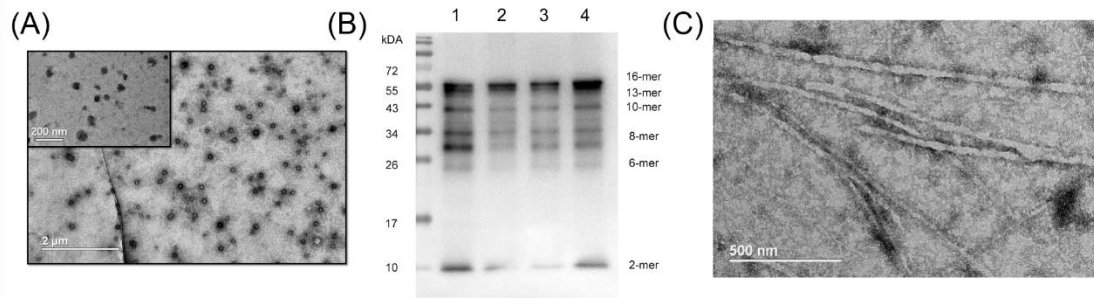
Figure S2. Characterization of amyloid oligomers and fibrils, Related to Figure 2. Initial stock solution monomeric Aβ40 at 100 µM was incubated in an Eppendorf tube at room temperature. Samples were taken from the stock solution at 1h. (A) TEM image of Aβ40 oligomer. (B) Western blot analysis of Aβ40 oligomer. The experiments were repeated for four times independently. Western blot analysis was visualized by EP1876Y primary rabbit antibody (Abcam). (C) TEM images of preformed Aβ40 fibrils (seeds). Samples were collected from the ThT fluorescence experiment after the verification of the formation of fibrils.

Name	Sequence
cHASI-1	FITC-βA-cyclo(isoD-**F**-R-Dap)-D-**V**-R-A-E-R-A-E
F4A	FITC-βA-cyclo(isoD-**A**-R-Dap)-D-V-R-A-E-R-A-E
V8A	FITC-βA-cyclo(isoD-F-R-Dap)-D-**A**-R-A-E-R-A-E
F4A/V8A	FITC-βA-cyclo(isoD-**A**-R-Dap)-D-**A**-R-A-E-R-A-E
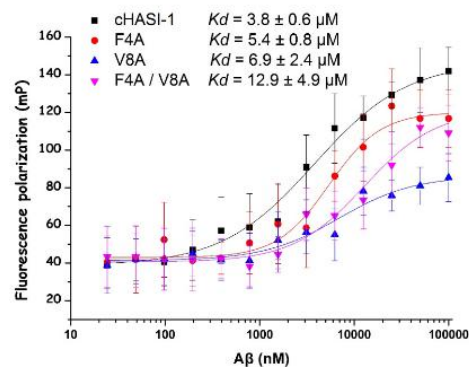
Figure S3. Affinity of hydrophobic mutants (F4A, V8A and F4A/V8A) of cHASI-1 for fibril surface, Related to Figure 2. Fluorescence polarization assay showing binding affinity of the 20 nM FITC-labeled peptides to 100 µM fibril-containing solution of Aβ40. Buffer: 20 mM sodium phosphate buffer (pH 7.4) supplemented with 200 µM EDTA and 0.02% NaN$_3$. Error bars represent standard deviation from the mean of three independent experiments.
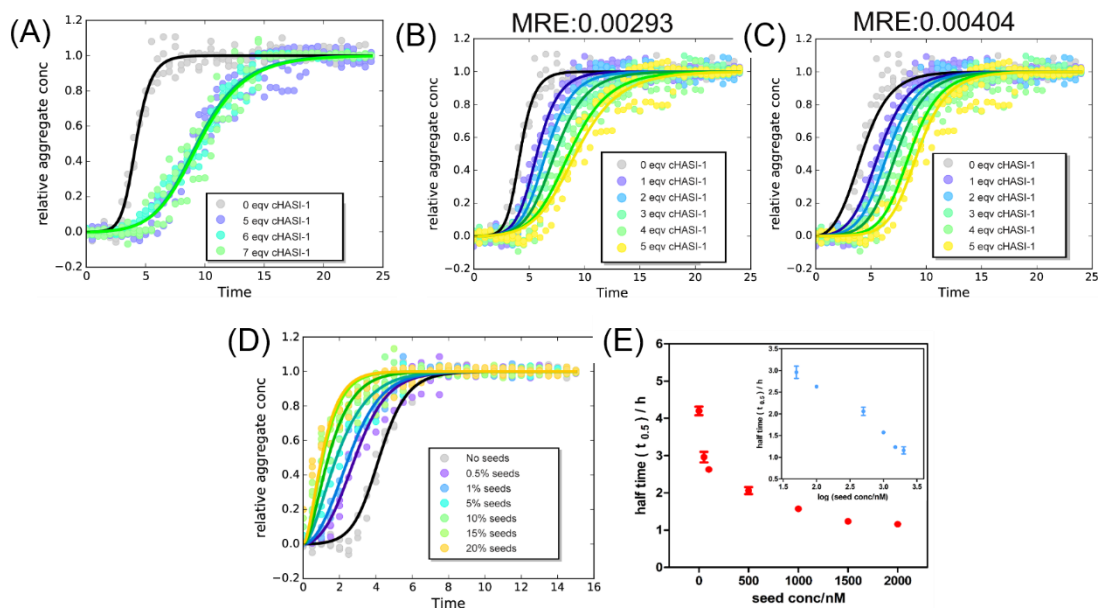
Figure S4 Aggregation kinetics of Aβ40, Related to Figure 6. (A) Saturation effect of cHASI-1 at high concentrations. Kinetics of 10 µM Aβ40 aggregation in the presence of 5 to 7 molar equivalents (50-70 µM) of cHASI-1 relative to Aβ40. Buffer: 20 mM sodium phosphate buffer (pH 7.4) supplemented with 200 µM EDTA and 0.02% NaN₃ with 20 µM ThT. All the data show three technical replicates overlaid. (B-C) Fitting of kinetic curves of Aβ40 aggregation in presence/absence of cHASI-1. The dots represent the data from the experiments carried out in current study, while the lines are fitting of the kinetic curves with different sets of parameters. The MRE (mean residual error) of fitting is denoted above each figure. (D) Aggregation kinetics of 10 µM Aβ40 solution in the absence and presence of 0.5%, 1%, 5%, 10%, 15% and 20% of preformed seed fibrils. (E) Half time for aggregation of 10 µM Aβ40 on the concentration of preformed seeds. Error bars represent SEMs of three replicates from (D). The inset shows the same data plotted versus the logarithm of seed concentration.
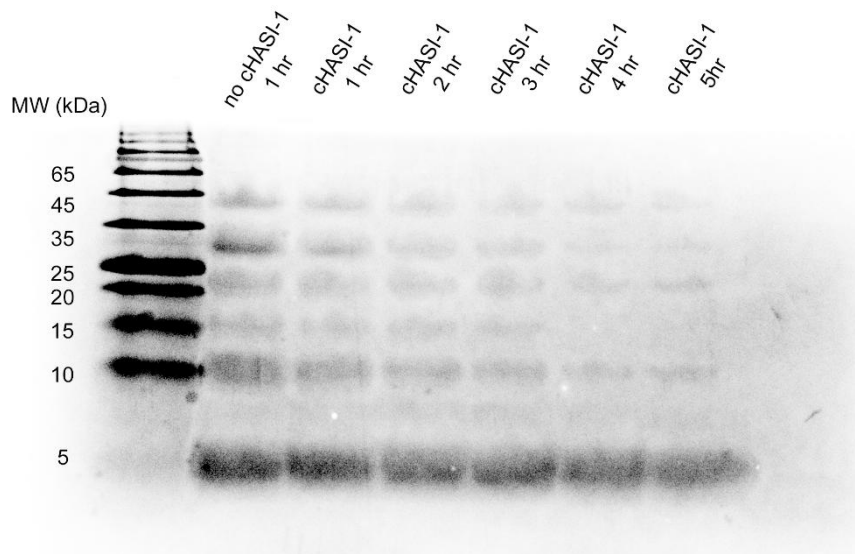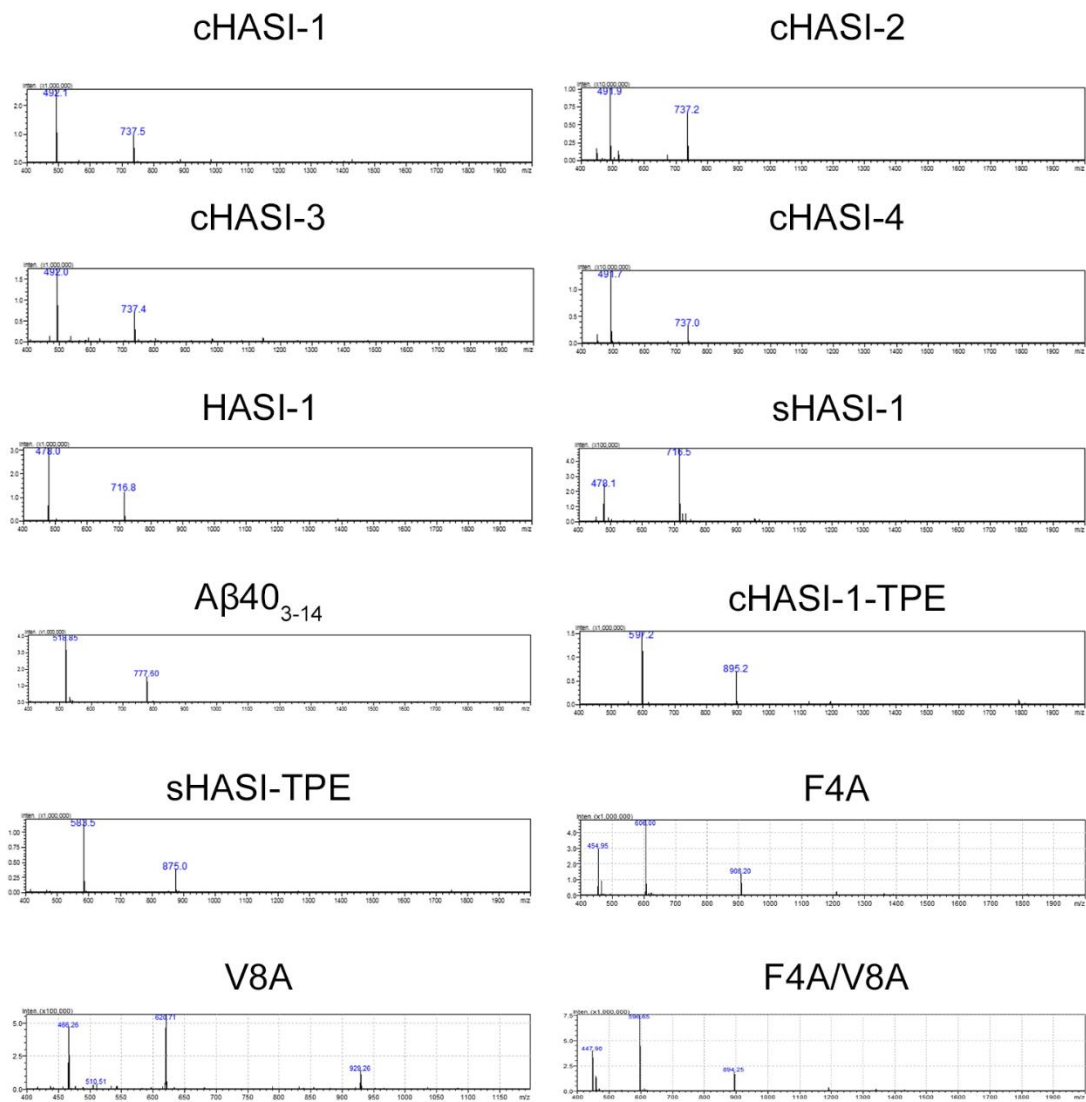
Figure S5. SDS-PAGE showing the amounts of Aβ40 oligomers in the absence or presence of cHASI-1, Related to Figure 7. Initial concentration of Aβ40 monomers and cHASI-1 were 10 µM and 50 µM, respectively. Preformed fibrils (0.5 µM) were added to promote the oligomerization. The aggregation reaction was quenched at *t=1, 2, 3, 4, and 5h* by adding loading buffer (containing 4% β-mercaptoethanol). 30 µL of each solution was analyzed by SDS-PAGE and subsequently silver staining following Silver Staining Protocol (Invitrogen.)
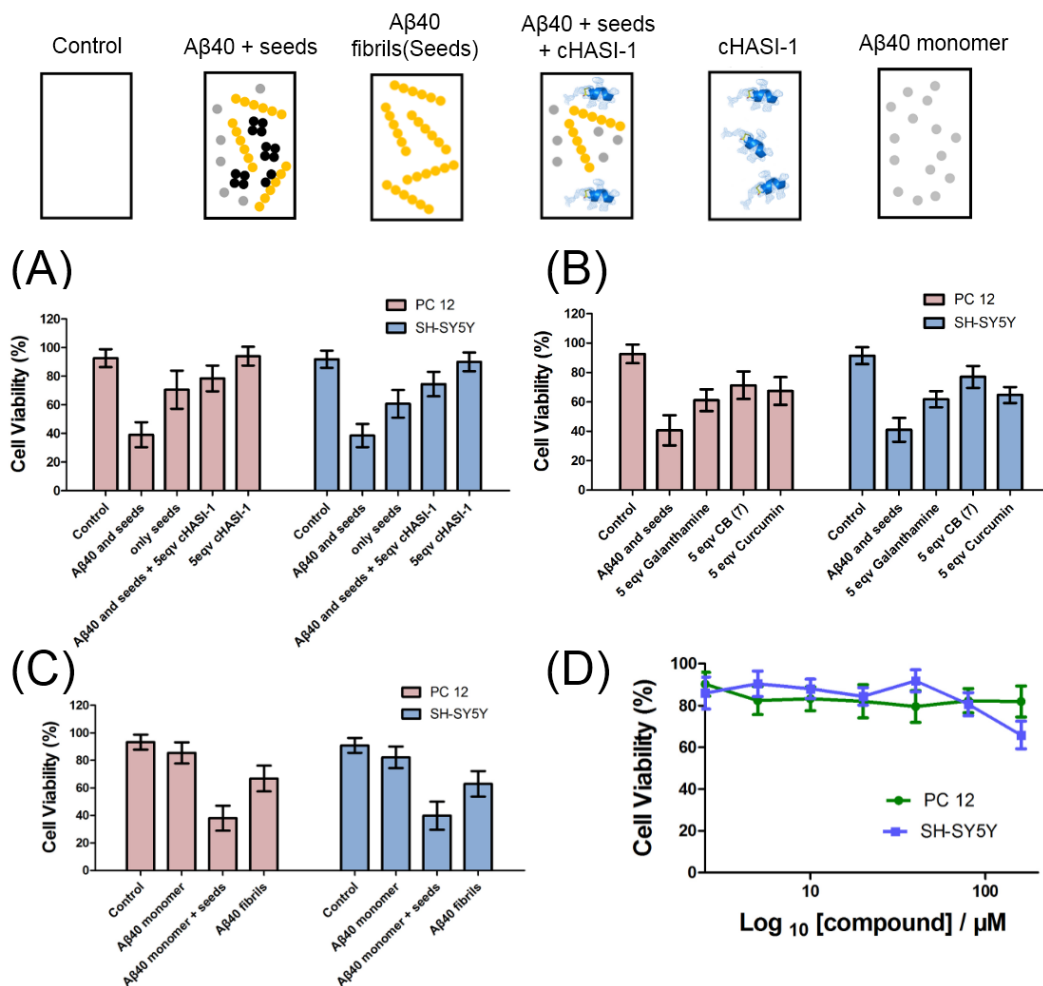
Figure S6. Cell Viability of PC12, SH-SY5Y treated with different conditions, Related to Figure 7. (A) Viability of PC12 and SH-SY5Y treated with preformed Aβ40 fibrils (0.5 µM) in presence of fresh monomer (10 µM), preformed Aβ40 fibrils (0.5 µM), preformed Aβ40 fibrils (0.5 µM) and fresh monomer (10 µM) in presence of 50 µM cHASI-1 as well as only 50 µM cHASI-1. The average and standard deviations shown are over four replicates of each condition. (B) Viability of PC12 and SH-SY5Y treated with preformed Aβ40 fibrils (0.5 µM) and dfresh monomer (10 µM) in the absence or presence of 50 µM Curcumin, Galanthamine, and Cucurbit [7] uril respectively. The average and standard deviations shown are over four replicates of each condition. (C) Viability of PC12 and SH-SY5Y treated with fresh monomer (10 µM) in the presence or absence of preformed Aβ40 fibrils (0.5 µM), as well as only preformed fibrils (10 µM). The average and standard deviations shown are over four replicates of each condition. (D) Viability of PC12 and SH-SY5Y cells treated with 2.5-160 µM cHASI-1. Error bars represent SEMs of at least three independent measurements.
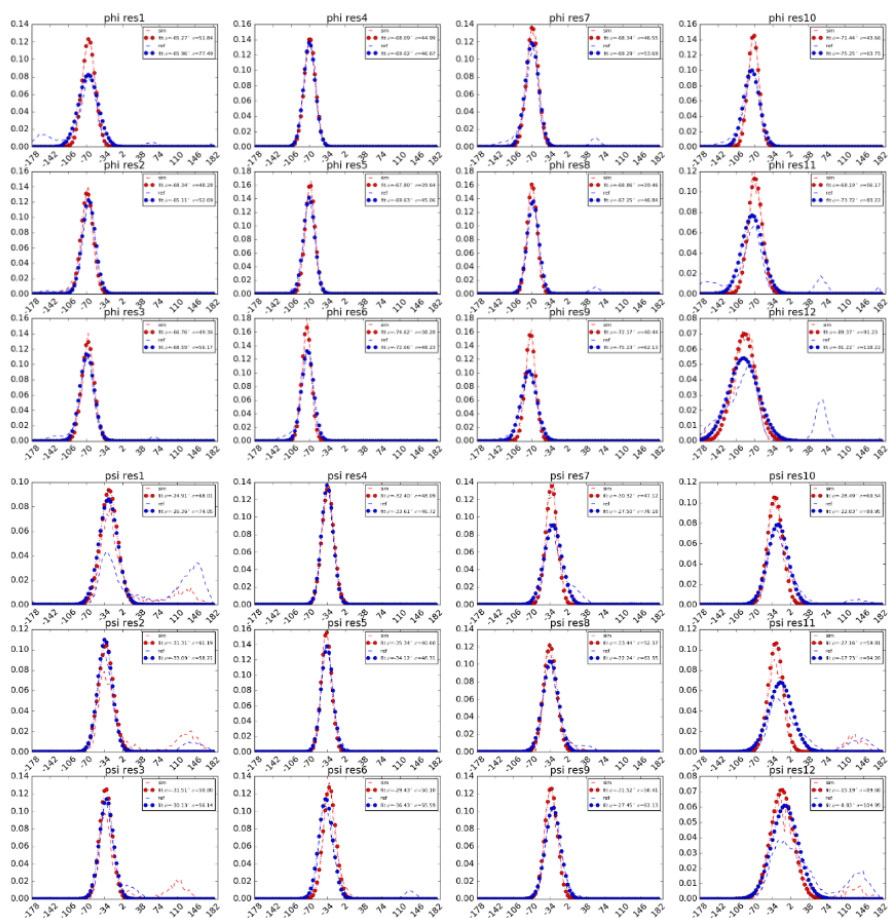
Figure S7. Distributions of dihedrals of cHASI-1 those obtained according to of bound helical conformations of HASI-1, Related to Figure 4. The upper three panels show the individual dihedral distribution of φ angles in the peptide, where the blue dots represent the target distribution which is obtained from the bound helical conformation in HASI-1 and red ones denote the dihedral distribution with optimized dihedral parameters. All the distributions are fitted with Gaussian distribution, as shown with lines. And the mean and variance of each Gaussian distribution is noted in the legend. The lower three panels are the dihedral distribution of Ψ angles in the peptide. The results of the dihedral distributions for cHASI-2 to 4 are similar to those of cHASI-1 and are not displayed due to space limitations.

cHASI-1

cHASI-2

cHASI-3

cHASI-4

HASI-1

sHASI-1

Aβ40$_{3-14}$

cHASI-1-TPE

sHASI-TPE

F4A

V8A

F4A/V8A

Figure S8. MS Spectra of cHASIs, Related to Table 1.

Transparent Methods

Abbreviations

Fmoc, 9-fluorenylmethyloxycarbonyl; HCTU, 2-(1H-6-chlorobenzotriazol-1-yl)-1,1,3,3-tetramethyl uranium hexafluorophosphate; DIPEA, diisopropylethylamine; DMF, dimethylformamide; ESI-MS, electrospray ionization mass spectrometry; RP-HPLC, reserved-phase high performance liquid chromatography; RT, room temperature; SPPS, solid-phase peptide synthesis; FITC, fluorescein isothiocyanate; TFA, trifluoroacetic acid; TIS, triisopropylsilane; Et$_2$O, diethyl ether; LC-MS, liquid chromatography–mass spectrometry; HPLC, high-performance liquid chromatography;

Materials

All solvents and reagents used for solid phase peptide synthesis were purchased from commercial suppliers including GL Biochem (Shanghai) Ltd., Shanghai Hanhong Chemical Co., J&K Co. Ltd., Shenzhen Tenglong Logistics Co. or Energy Chemical Co. and were used without further purification unless otherwise stated. Aβ40 (DAEFRHDSGY / EVHHQKLVFF / AEDVGSNKGA/ IIGLMVGGVV) was synthesized by Shanghai Top-peptide Biotechnology Co., Ltd. The appearance of the product is white powder and the purity is above 95% (95.74%) (See Appendix). Further purification of Aβ40 was conducted by FPLC before each experiment. (Scheme S1)

HPLC and Mass spectrometry

Peptides were analyzed and purified by HPLC (SHIMAZU Prominence LC-20AT) using a C18 analytic column (Agilent ZORBAX SB-Aq, 4.6 × 250 mm, 5 μm, flow rate 1.0 mL/min) and a C18 semi-preparative column (Agilent Eclipse XDB-C18, 9.4 × 250 mm, 5 μm, flow rate 5 mL/min). H$_2$O (containing 0.1% TFA) and pure acetonitrile (containing 0.1% TFA) were used as solvents in linear gradient mixtures. LC-MS spectra were carried out on SHIMAZU LC-MS 8030 (ESI-MS).

Peptide Synthesis and Characterization (Figure 2) (Shepherd et al., 2005)

SPPS was performed by standard protocol mentioned in general information. Peptide synthesis was performed manually on Rink Amide AM resin (loading capacity: 0.54 mmol/g) (GL Biochem Ltd.) by standard Fmoc-based solid-phase peptide synthesis. Generally, Rink amide AM resin was pre-swelled with DCM/NMP (1/1) for 30 min. Fmoc deprotection was performed with morpholine (50% in NMP) for 30min × 2. Then the resin was washed with NMP (5 times), DCM (5 times) and NMP (5 times). Fmoc-protected amino acids (6.0 equiv according to initial loading of the resin) and HCTU (5.9 equiv) were dissolved in NMP, followed by DIPEA (12.0 equiv). The mixture was pre-activated for 1 min and added to the resin for 1-2 h, then the resin was washed with NMP (5 times), DCM (5 times) and NMP(5 times). The allyl ester and allyl carbamate were removed using Pd(PPh$_3$)$_4$ (0.1 eq) and N,N-dimethylbarbituric acid (4 eq), in DCM for 2 h for 2 times. Cyclization was performed on the resin using PyBOP/HOBt/NMM (2:2:2.4 eq) in DMF. Upon completion of peptide assembly, peptides were N-terminally acetylated with a solution of acetic anhydride and DIPEA in NMP (1: 1: 8 in volume) for 1h. TPE labelling was performed on the resin with the solution of TPE (4 eq), HCTU and DIPEA for 2h for 2 times. FITC labelling

was performed on the resin with the solution of FITC (isomer I, 4 eq) and DIPEA (14 eq) in DMF overnight. Peptides were cleaved from the resin with a mixture of TFA/H_2O/EDT/TIS (94:2.5:2.5:1) for 2 h and concentrated under a stream of nitrogen. The crude peptides were then precipitated with Hexane/Et_2O (1:1 in volume) at -20°C, isolated by centrifugation then dissolved in water/acetonitrile, purified by semi-preparative HPLC and analyzed by LC-MS. Analytical data are shown in Supporting Table S1.

Circular Dichroism Spectroscopy (CD)

CD spectra were obtained using a Chirascan Plus Circular Dichroism Spectrometer at 298 K. Peptides were dissolved in ddH$_2$O, pH 7.0, at concentrations of 100 µM. Parameters used in the experiment are as followed: wavelengths from 190 to 250 nm were measured with resolution of 0.5 nm, response of 1 s, bandwidth of 1 nm, scanning speed of 20 nm/min. Each spectrum represents the average of two scans and smoothed using Pro-Data Viewer by Applied Photophysics with smooth window of 10. CD data are presented as mean residual elipticity [ ] in deg·cm^2 ·dmol^{-1} using the equation $[\theta] = \theta/(10 \times C \times Np \times l)$, where θ is the ellipticity in milidegrees, C is the peptide molar concentration (M), l is the cell path length (cm), and Np is the number of peptide units. Percent helicity was calculated based on the equation described by Arora(Wang et al., 2006): Helicity% = $[\theta]_{222}/[\theta]_{max} \times 100$, where $[\theta]max = (-44\,000 + 250T)(1 - k/n)$ for k = 4.0 and n = number of amino acid residues in the peptide, T = 25 °C.

Preparation of monomeric Aβ40 samples.(Cohen et al., 2015; Habchi et al., 2017)

Solutions of monomeric Aβ was prepared by dissolving the Aβ40 peptide in 6 M GuHCl. Monomeric forms were purified by the use of a Superdex 75 10/300 GL column (GE Healthcare) at a flow rate of 0.3 mL·min^{-1}, and were eluted in 20 mM sodium phosphate buffer (pH 7.4) supplemented with 200 µM EDTA and 0.02% NaN$_3$. The center of the peak was collected, and the peptide concentration was determined from the absorbance of the integrated peak area using ε280 = 1,490 L·mol^{-1}·cm^{-1}.
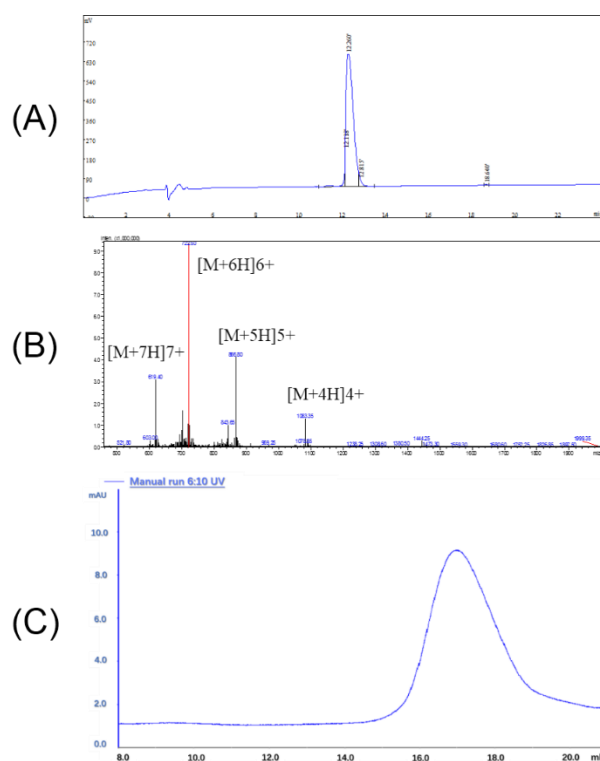
Scheme S1. Characterization of Aβ40 monomer, Related to Figure 6. (A) HPLC trace of the Aβ40 product at different UV irradiation times, monitored at 214 nm. Purification Condition: Column, 4.6*150 mm, kromasil C18-5. Solvent A, 0.1%Trifluoroacetic in 100% Acetonitrile. Solvent B, 0.1%Trifluoroacetic in 100% Water. Gradient, 0.01min 5% A and 95% B, 25.00min 70% A and 30% B. Flow rate, 1ml/min. Injection volume, 10 μL. (B) MS Spectra of Aβ40. (C) Size exclusion chromatograms obtained during the Aβ40 monomer purification process used in these studies.

Thioflavin-T (ThT) Fluorescence Assay.
The kinetics of Aβ aggregation was monitored by the binding of thioflavin T (ThT) to β-sheet-rich amyloid aggregates as previously report.(Cohen et al., 2015; Cukalevski et al., 2015; Habchi et al., 2017) The obtained monomer was diluted with buffer to the desired concentration. Each sample contains 10 μM Aβ monomer in the absence or presence of 10 μM, 20 μM, 30 μM, 40 μM, 50 μM cHASI-1 with 20 μM ThT. All samples were prepared in low-binding Eppendorf tubes on ice using careful pipetting to avoid introduction of air bubbles. Each sample was then pipetted into multiple wells of a 96-well half-area, low-binding, clear-bottomed PEG coating plate (Corning 3881), at 90 μL per well. Fluorescence of ThT was measured with excitation wavelength of 440 nm and emission wavelength of 490 nm. The fluorescence intensity was measured on a microplate reader every 30 minutes from 0 h to 35 h. For the seeded experiments(Cukalevski et al., 2015), preformed fibrils were prepared through the procedure reported previously by Linse et al. Specifically, the seed sample was taken from the solution that was used, as described above, to monitor Aβ40 aggregation kinetics at t= 24h. To ensure that the aggregation reaction was complete, we analyzed the morphologies of aggregates using TEM. (Figure S2C) Then the seed sample were then added to freshly prepared monomer to reach a 0.5%, 1%, 5%, 10%, 15% and 20% final concentration of seeds.

Samples were then collected from the wells into low-binding tubes on ice and used within a few hours. In all cases, cHASI-1 was previously dissolved in 100% DMSO to a concentration of 10 mM, and then diluted in the peptide solution to reach a final DMSO concentration (maximum of 0.5%) less than 1%. It is proved that the addition of 1% DMSO in the reaction mixture has no effect on Aβ aggregation.(Habchi et al., 2017)

Fluorescence Polarization Assay (FP) (Wallin et al., 2018)

Different aggregation species of Aβ40 were prepared as previous report.(Wallin et al., 2018) An initial stock solution monomeric Aβ40 at 100 μM was incubated in an Eppendorf tube at room temperature. Samples were taken from the stock solution at different time points (i.e., 0, 1 and 24 h), where the different aggregation species of monomers, oligomer and fibrils. Fluorescence polarization experiments were performed in 96-well plates on plate reader (Perkin Elmer, Envision, 2104 multilabel reader) at 25 °C with excitation at 485 nm and emission at 520 nm. Concentration of the peptides were determined by 495 nm absorption of FITC. Briefly, FITC-labeled peptides were mixed with increasing concentration of different Aβ species to a final peptide concentration of 20 nM. The mixture were then incubated at 4 °C for 1h in the dark. The binding affinity (K_d) values were determined by plotting the fluorescence polarization data to concentrations of respectively incubated proteins using nonlinear regression analysis by Origin 7.0.

Isothermal Titration Calorimetry (ITC).(S and AD, 2017)

The binding affinities between Aβ40 monomers or fibrils and the peptides were measured using ITC. All experiments were performed with an ITC microcalorimeter (MicroCal iTC200) at 25 °C. For each injection, 2 μL of different concentration of peptides inhibitor candidate was titrated into10 μM Aβ40 monomers or fibrils in buffer of 20 mM sodium phosphate buffer (pH 8) supplemented with 200 μM EDTA and 0.02% NaN_3. The binding data was fitted using the software ORIGIN 7.0.

Cell Viability by MTT Assay.(Cohen et al., 2015)

Human embryonic kidney cell line (CRL-3216, American Type Culture Collection), were maintained in Dulbecco's modified Eagle's medium (DMEM, Gibco); Human pheochromocytoma cell line, PC12 (CRL-1721, American Type Culture Collection) were maintained in RPMI-1640 Medium; Human neuroblastoma cell line, SH-SY5Y (CRL-2266, American Type Culture Collection) were maintained in 1:1 mixture of ATCC-formulated Eagle's Minimum Essential Medium and F12 Medium. All the medium were supplemented with 10% (v/v) fetal bovine serum (FBS, Gibco) and penicillin/streptomycin (100 μg/mL, Gibco). Cells were cultured at 37 °C in a humidified atmosphere with 5% CO_2. Liver-derived cell lines QSG-7701 (Institute of Cytology, Chinese Academy of Sciences, Shanghai, China) were maintained in DMEM medium (Gibco) supplemented with 10% (v/v) FBS (Gibco). The day before peptide treatment, cells were seeded onto 96-well plates in DMEM medium with 10% FBS to give 30% − 50% confluence.

In Figure 7B, cell viability upon treatment of 10 μM Aβ40 monomers and 0.5 μM preformed fibrils in the absence or presence of 10, 20, 50 μM cHASI-1. In Figure S6A, cell viability upon treatment of 10 μM Aβ40 monomers in the presence of 0.5 μM preformed fibrils, 0.5 μM

preformed fibrils, 10 µM Aβ40 monomers and 0.5 µM preformed fibrils in presence of 50 µM cHASI-1, 50 µM cHASI-1 separately. In Figure S6B, cell viability upon treatment of 10 µM Aβ40 monomers and 0.5 µM preformed fibrils in the absence or presence of 50 µM Curcumin, Galanthamine, and Cucurbit [7] uril respectively. In Figure S6C, cell viability upon treatment of 10 µM fresh Aβ40 monomers, 10 µM fresh Aβ40 monomers in the presence of 0.5 µM preformed fibrils, 10 µM preformed fibrils. After that cells were cultured for another 24 h. Subsequently, they were determined by the MTT assay.

To explore the cytotoxicity of cHASI-1, we incubate 2.5, 5, 10, 20, 40, 80, 160 µM cHASI-1 with two normal cells including 293T and Chang liver as well as PC12 and SH-SY5Y in Figure 7D and Figure S6D . After 48 h incubation at 37 °C, 20 µL of MTT reagent was added and incubated at 37 °C for another 4 h. Then the medium was removed, and the formazan product was dissolved in 150 µL of DMSO. The absorbance at 570 nm of dissolved product was measured by a microplate reader (PerkinElmer, Envision). Cell viability (%) was determined relative to that of cells treated with a volume of PBS equal to the protein samples added.

Dot-Blot Assay(Cohen et al., 2015)

Aggregation was monitored by ThT fluorescence for samples of 10 µM Aβ40 with 0.5 µM of preformed seeds with and without 50 µM cHASI-1. Samples were taken from reactions without cHASI-1 after 1 hour, and from reactions with cHASI-1 after 1, 2, 3, 4 and 5 hour. The samples were collected from the incubation system and immediately injected into a Superdex 75 column. Eluted fractions (1 mL per fraction) were pooled into three section: monomers (elution volume between 15.5 and 19 ml), small oligomers (elution volume between 12 and 15.5 ml) and large oligomers (elution volume between 9 and 12 ml). The collected samples were spotted onto a nitrocellulose membrane (0.2 µm), and the membranes were dried and then blocked with EP1876Y primary rabbit antibody (Abcam). Alexa Fluor 488-conjugated secondary antibodies (Life Technologies) were subsequently added, and fluorescence detection was performed using a Typhoon Trio Imager (GE Healthcare).

PACE force field

All simulations in this manuscript were carried out using the PACE force filed, which represents systems at hybrid resolutions.(Han and Schulten, 2012, 2013; Qi et al., 2014) Proteins are described with a united-atom model in which hydrogen atoms are merged to their nearest heavy atoms except for those attached to amide groups. Solvent molecules and ions are represented with the MARTINI coarse-grained (CG) force field (Marrink et al., 2007). The use of the MARTINI greatly accelerates simulations. The potential energy of the PACE is expressed as follows:

$$U = U_{\text{bond}} + U_{\text{angle}} + U_{\text{dihedral}} + U_{\text{improper}} + U_{\phi,\psi,\chi1} + U_{\text{LJ}} + U_{\text{ele}} + U_{\text{polar}} + U_{\text{MARTINI}} + U_{\text{UA−MARTINI}} \quad [\text{S1}].$$

In the potential energy function above, the first five terms describe geometry of proteins and the conformational preference of their backbone and side chains. U_{LJ}, U_{ele} and U_{polar} describe non-bonded van der Waals, electrostatic and polar interactions, respectively, between protein sites. U_{MARITNI} comprises the energy terms from the standard MARTINI while $U_{\text{UA-MARTINI}}$

describe the interactions between sites at different resolutions. Details of these energy terms and their parameterization can be found elsewhere (Han and Schulten, 2012, 2013; Qi et al., 2014). The PACE has been applied to the studies of large conformational changes of proteins and protein-protein interactions. This model has been used to fold multiple proteins into their native structures(Han and Schulten, 2012, 2013), to reproduce experimental structural features of disordered proteins like Aβ (Jiang et al., 2018) and alpha-synuclein (Yu et al., 2015), and to predict correctly the binding thermodynamics between Aβ40 peptides(Cao et al., 2017), the kinetics of Aβ17-42 fibril elongation(Han and Schulten, 2014) as well as the affinity of peptides for Aβ40 fibril surface as shown in our previous and current study(Jiang et al., 2018).

Parameterization for modeling helical stabilized peptides

The force field parameters for the TD linker are currently unavailable. To simulate the binding of helical peptides stabilized by the linker, we mimic the effect of the linker by applying the following harmonic restraints on backbone dihedrals of peptides (φ, ψ):

$$E_{\mathrm{hel}} = \sum_i K_i(\varphi_i - \varphi_{i0})^2 + \sum_j F_j\left(\psi_j - \psi_{j0}\right)^2 \quad [\mathrm{S2}]$$

where K_i and F_j are the force constants of restraints applied on individual dihedrals φ and ψ, respectively, and φ_{i0} and ψ_{j0} are corresponding equilibrium values. We optimized these parameters by fitting dihedral distributions obtained with a group of helical conformations of the linear HASI-1 bound on Aβ fibril surface collected from the equilibrium binding simulations of this peptide (Figure S7). A HASI conformation was considered to be helical if there are at least eight residues in a helical state. Residue i was thought to be in a helical state if the backbone dihedrals (φ,ψ) of residues i-1, i and i+1 are all within (-60°±30°, -47°±30°). The optimized parameters are summarized in Table S2. Of note, the parameters for each of the four cyclic variants of HASI-1, namely cHASIs (1 to 4), were optimized separately but for all variants, the same set of dihedral distributions of HASI-1 were used in fitting. Here, we assumed that these variants have a similar helical character, which is supported by our CD measurements (Figure 2C-D).

Simulation models and setup

The model of Aβ40 fibril was built by duplicating the fibrillar chain along z axis with an interval of 0.49 nm. The unit fibrillar chain is extracted from a solid-state NMR structure (PDB id: 2lmn) of Aβ40 fibrils. The fibril model we built contains 12 fibril chains and is put in the center of cubic simulation box with its fibril axis parallel to the *z* axis. Following our previous study (Jiang et al., 2018), we adjusted the spacing in the *z* direction so that the peptide chains in our model is able to form continuous fibrillar structures with their nearest neighbors owing to the periodic boundary conditions. This model avoids the presence of fibril tips and ensures that other peptides can only bind to the fibril surface.

Initial conformations of each cyclic peptide were randomly selected from a 50-100ns normal simulation. For each simulation replica, a cyclic-peptide was placed with a random orientation in a box containing the fibril., The minimum atomic distance between the cyclic peptide and the fibril is longer than 1.5 nm. The distance of the center of the cyclic peptide to the fibril axis is

kept at > 3.5 nm.

The replica exchange molecular dynamics (REMD) technique was employed to enhance sampling (Sugita and Okamoto, 1999). For each system, 48 parallel simulations, each starting with a different structure prepared as above, were conducted at temperatures of 330-690K. Each replica simulation lasted for 1.4 μs. The accumulated simulation time for all six systems studied here, namely Aβ$_{3-14}$, HASI-1, and cHASIs-1/2/3/4, was over 400 μs. The exchange between replicas was attempted every 3.5 ps with an acceptance ratio

$$p = min\left(1, e^{(E_j - E_i) \times \left(\frac{1}{k_B T_i} - \frac{1}{k_B T_j}\right)}\right) \text{ [S3],}$$

where E_i and E_j are total energy of replicas i and j, and T_i and T_j are the corresponding simulation temperature. In this study, the acceptance ratio was not less than 30%.

During the REMD simulations, harmonic restraints were applied to fix the positions of backbone atoms of the fibril and those of side chains buried inside the fibril. These restraints prevented the deformation of fibril structures in simulations at high temperature. No positional restraints were applied on side chains on the fibril surface as the flexibility of these side chains could be essential for peptide binding.

All the above simulations were performed with the GROMACS 5 software package (Abraham et al., 2015). Non-bonded interactions were cut off at 1.2 nm and smoothed with a switching function. The Nose-Hoover thermostat was used to maintain simulation temperature (Nosé, 1984). The timestep of simulations was 3.5 fs, a typical value of PACE simulations (Han and Schulten, 2012).

Affinity calculation

The binding affinity of cyclic-peptides on fibril surface was used to monitor the simulation convergence. The binding affinity was calculated as:

$$\Delta G_{sim} = RT ln \frac{[U]}{[B]} \text{ [S4],}$$

where R is the gas constant, T is the temperature, and [U] and [B] are the fraction of unbound and bound states in the simulation, respectively. To estimate [U] and [B], we first defined the bound and unbound states using the distance (r) of the mass center of peptides to the fibril axis. If r < 2.6 nm, the peptide was thought to be bound; if r is between3 nm and 4 nm, the peptide was thought to be detached.

As shown in Figure S1G, the binding affinity of the peptides changed greatly over the first 700 ns simulations but much less so after t =700 ns, indicating that after this time point, the simulation results were likely converged. As such, the first 700 ns simulation was discarded for further analysis.

To calculate the affinity at a temperature not covered in our simulations, we first fit the simulated binding affinity at different temperatures to a two-state model whose thermodynamic behavior is described as follows:

$$\frac{\Delta G}{RT} = \frac{\Delta H}{R}\frac{1}{T} - \frac{\Delta S}{R} \quad \text{[S5]},$$

where ΔG is the binding free energy, and ΔH and ΔS are change in enthalpy and entropy during the binding process. The fitting of affinity data to the two-state model was shown in Figure S1A-F. Once ΔH and ΔS have been determined, ΔG at any given temperature can be estimated.

To facilitate a direct comparison with experimental data, we also converted the calculated affinities to the corresponding values at standard concentration (1 M). The standard binding free energy (ΔG_0) was obtained by adding to ΔG a term $-k_B T \ln\frac{V_{\text{unbound}}}{V_{\text{ref}}}$ that accounts for difference in peptide concentration between the simulations and experiments. In this correction term, $V_{unbound}$ is the volume of unbound state, which was estimated in current study to be ~128 nm³ and V_{ref} is the reference volume and takes a value of 1.66 nm³ at 1M.

Kinetic data fitting

To probe the possible mechanism whereby cHASI-1 affected Aβ aggregation, we fit our kinetic data of Aβ aggregation to the master equation proposed by Meisl *et al.*(Meisl et al., 2016) that relates the change of normalized mass of aggregates over time to the rate constants of oligomerization in solution (k_n) or on fibril surface (k_2) and fibril elongation (k_+) as well as the concentration (K_M) of monomers needed to saturate fibril surface. This equation is expressed as follows:

$$\frac{M(t)}{M(\infty)} = 1 - \alpha\left(\frac{B_+ + C_+}{B_+ + C_+ e^{kt}}\frac{B_- + C_+ e^{kt}}{B_- + C_+}\right)^{\frac{\kappa_\infty^2}{\kappa\widetilde{\kappa_\infty}}}e^{-\kappa_\infty t} \quad \text{[S6]}$$

where $B_\pm$, $C_\pm$, k, κ_∞ and $\widetilde{\kappa_\infty}$ are the functions of $k_n k_+$, $k_+ k_2$ and K_M.

Regardless of whether or not the inhibitor is present, the kinetic data of Aβ aggregation should always be able to be fit to the above equation, yielding the parameters for k_n, k_+, k_2 and K_M. In the presence of the inhibitor, the fitting gives the apparent values for these parameters that take into account the influence of the inhibitor. To probe if the inhibitor acts on a particular microscopic event of the aggregation process, we assumed the rate constants of the other two events are unaffected by the inhibitor and can be globally fit to all sets of kinetic data whereas the rate constant for the microscopic event of interest will be affected differently in the presence of the inhibitor at different concentrations. In the actual fitting, the products of k_n and k_+ as well as the product of k_2 and k_+ are adjustable parameters. Here, we assumed that k_+ will be constant regardless of the inhibitor concentration as our seeded kinetic experiment clearly showed that the inhibitor does not affect the fibril growth. Thus, if we want to test whether the inhibitor acts on the oligomerization in water, we can allow $k_n k_+$ to vary with the inhibitor concentration while globally fitting $k_2 k_+$ as well as K_M.(Meisl et al., 2016) Similarly, whether the inhibitor acts on the oligomerization on the amyloid surface can also be examined.

All the fitting was conducted on the webserver AmyloidFit (http://www.amylofit.ch.cam.ac.uk/). As shown in Figure S4B when the inhibitor was assumed to act on the surface-catalyzed oligomerization process, the fitting gave a smaller mean residual error (0.00293 versus 0.00404,

respectively) as compared to the fitting result when the inhibitor was assumed to act on the solution oligomerization (Figure S4C). Taken together, our fitting suggested that the inhibitor acts more likely on the surface-catalyzed oligomerization process than on the oligomerization in solution. Our fitting suggested that the inhibitor acts more likely on the surface-catalyzed oligomerization process than on the oligomerization in solution.

SDS-PAGE gel electrophoresis assay
Aggregation samples of 10 µM Aβ40 with 0.5 µM of preformed seeds with and without 50 µM cHASI-1. Samples were taken from reactions without cHASI-1 after 1 hour, and from reactions with cHASI-1 after 1, 2, 3, 4 and 5 hour. The samples were collected from the incubation system and immediately quenched by adding loading buffer (containing 4% β-mercaptoethanol). 30 µL of each solution was analyzed by SDS-PAGE and subsequently silver staining following Silver Staining Protocol (Invitrogen.)

Transmission Electron Microscopy (TEM)(Choi et al., 2017)
Samples for TEM were prepared following a previously reported method. Glow discharged grids (Formvar/Carbon 300-mesh, Electron Microscopy Sciences, Hatfield, PA, USA) were treated with samples from either with or without cHASI-1 incubation system (5 µL) for 2 min at room temperature. Excess sample was removed with filter paper and the grids were washed with ddH2O three times. Each grid was stained with uranyl acetate (1% w/v ddH2O, 5 µL) for 1 min. Uranyl acetate was blotted off and grids were dried for 20 min at room temperature. Images of samples were taken by a JEOL JEM-2100 TEM system (120 kV, 25,000× magnification).

Supplemental References
Abraham, M.J., Murtola, T., Schulz, R., Páll, S., Smith, J.C., Hess, B., and Lindahl, E. (2015). GROMACS: High performance molecular simulations through multi-level parallelism from laptops to supercomputers. SoftwareX 1, 19-25.
Cao, Y., Jiang, X., and Han, W. (2017). Self-Assembly Pathways of beta-Sheet-Rich Amyloid-beta (1-40) Dimers: Markov State Model Analysis on Millisecond Hybrid-Resolution Simulations. J. Chem. Theory. Comput. 13, 5731-5744.
Han, W., and Schulten, K. (2014). Fibril elongation by Abeta (17-42): kinetic network analysis of hybrid-resolution molecular dynamics simulations. J. Am. Chem. Soc. 136, 12450-12460.
Marrink, S.J., Risselada, H.J., Yefimov, S., Tieleman, D.P., and de Vries, A.H. (2007). The MARTINI force field: coarse grained model for biomolecular simulations. J. Phys. Chem. B. 111, 7812-7824.
Nosé, S. (1984). A molecular dynamics method for simulations in the canonical ensemble. Mol. Phys. 52, 255-268.
Qi, Y., Cheng, X., Han, W., Jo, S., Schulten, K., and Im, W. (2014). CHARMM-GUI PACE CG Builder for solution, micelle, and bilayer coarse-grained simulations. J. Chem. Inf. Model. 54, 1003-1009.
Kumar, S., Hamilton, A.D. (2017). α-Helix Mimetics as Modulators of Aβ Self-Assembly. J. Am. Chem. Soc. 139(16), 5744-5755.
Shepherd, N.E., Hoang, H.N., Abbenante, G., and Fairlie, D.P. (2005). Single turn peptide alpha helices with exceptional stability in water. J. Am. Chem. Soc. 127, 2974-2983.

Sugita, Y., and Okamoto, Y. (1999). Replica-exchange molecular dynamics method for protein folding. Chem. Phys. Lett. 314, 141-151.

Wang, D., Chen, K., Kulp, I.J., and Arora, P.S. (2006). Evaluation of biologically relevant short alpha-helices stabilized by a main-chain hydrogen-bond surrogate. J. Am. Chem. Soc.128, 9248-9256.

Yu, H., Han, W., Ma, W., and Schulten, K. (2015). Transient beta-hairpin formation in alpha-synuclein monomer revealed by coarse-grained molecular dynamics simulation. J. Chem. Phys. 143, 243142.